Periductal Fibroblast Density Defines Lymphocyte Exclusion via a CD44-Dependent Stromal Checkpoint in Pancreatic Cancer

Zoe X. Malchiodi[1*], Alexander A. Lekan[1*], Robert K. Suter[1], Atul Deshpande[2,3,4], Ivana Peran[1], Brent T. Harris[5,6], Anju Duttargi[5], Min-Ju Chien[1], Samika Hariharan[1], Lucia Wetherill[1], Selime Arslan[1], Sandra A. Jablonski[1], Won Jin Ho[2], Marwa Afifi[1], Elana J. Fertig[2,7,8,9], Louis M. Weiner[1]

[1] Department of Oncology, Georgetown Lombardi Comprehensive Cancer Center, Georgetown University Medical Center, Washington, DC, USA

[2] Department of Oncology, Sidney Kimmel Comprehensive Cancer Center, Johns Hopkins School of Medicine, Baltimore, MD, USA

[3] Department of Electrical and Computer Engineering, Johns Hopkins University, Baltimore, MD, USA

[4] Data Science and AI Institute, Johns Hopkins University, Baltimore, MD, USA

[5] Department of Pathology, Georgetown University Medical Center, Washington, DC, USA

[6] Department of Neurology, Georgetown University Medical Center, Washington, DC, USA

[7] Department of Applied Mathematics and Statistics, Johns Hopkins University Whiting School of Engineering, Baltimore, MD, USA

[8] Department of Biomedical Engineering, Johns Hopkins University School of Medicine, Baltimore, MD, USA

[9] Department of Medicine, University of Maryland School of Medicine, Baltimore, MD, USA

*These authors contributed equally to this work.

23 **Address correspondence to:** Louis M. Weiner, MD, Georgetown Lombardi Comprehensive

24 Cancer Center, Research Building E501, 3970 Reservoir Rd NW, Washington, DC, 20057.

25 E-mail: weinerl@georgetown.edu.

26 **Graphical Abstract**

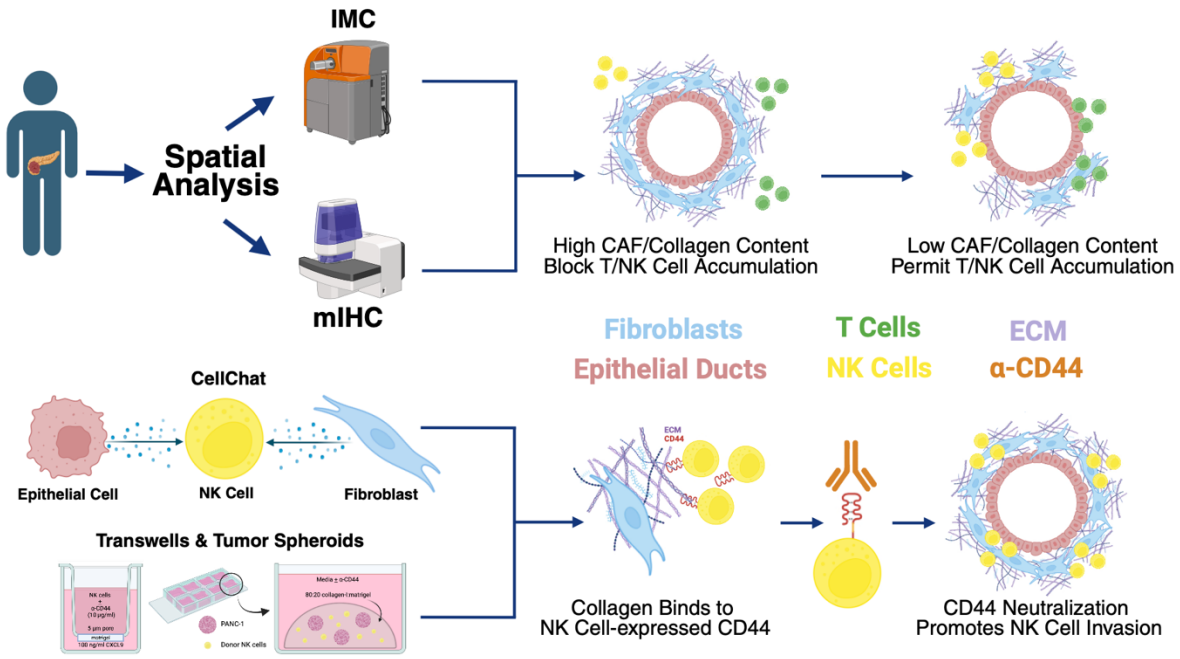

27

Abstract

Pancreatic ductal adenocarcinoma (PDAC) exhibits dense fibrosis and immune exclusion. While fibrosis has been studied globally and at the region-of-interest level, its impact on stromal-ductal architecture and immune cell localization remains unknown. Here, we establish cancer-associated fibroblast (CAF)-stratified ductal spatial architecture as a fundamental determinant of immune exclusion in PDAC. Focusing on malignant PDAC epithelial ductal regions, the critical interface where immune cells must access tumor epithelium, we demonstrate that periductal fibroblast organization dictates leukocyte proximity. Through integrative analysis of treatment-naïve patient samples from three independent cohorts – including imaging mass cytometry, multiplex immunohistochemistry, and single-cell RNA sequencing – we uncovered that activated, pro-inflammatory leukocytes preferentially localized near malignant ducts in regions with low fibroblast density. Stratifying epithelial-ductal regions by CAF abundance revealed a graded constraint: increasing fibroblast content corresponded to reduced leukocyte–epithelial proximity and elevated collagen I deposition. Despite their exclusion in high-CAF ducts, leukocytes in low-CAF ducts retained functional competence. Mechanistically, ligand–receptor inference implicated collagen–CD44 signaling as an adhesion axis anchoring immune cells within fibroblast-rich zones, with CD44 blockade enhancing natural killer cell invasion and motility in fibrotic spheroid models. Thus, by establishing ductal regions as critical spatial units of immune exclusion, these findings provide a framework for dissecting stromal–immune interactions and reveal targetable "stromal checkpoints" that can be leveraged to overcome CAF-driven barriers to leukocyte motility and infiltration in PDAC.

Introduction

Pancreatic ductal adenocarcinoma (PDAC) has a 5-year survival rate of 12%[1]. PDAC is considered to be an immunologically "cold" tumor with minimal infiltration by activated leukocytes and immunotherapy-based clinical trials using checkpoint inhibitors have been largely unsuccessful[2-4]. This resistance can be at least partly attributed to the tumor's desmoplastic stroma, driven by extracellular matrix (ECM) deposition from cancer-associated fibroblasts (CAFs)[5]. The resulting fibrotic barrier increases tissue stiffness while restricting activated leukocyte infiltration and access to malignant ductal epithelial cells[6, 7]. Therefore, defining how CAF spatial organization within the periductal stroma constrains activated leukocyte-epithelial cell interactions is critical to creating successful immune-based therapeutic approaches.

Recent studies have explored the impact of CAFs on tumor cell progression in PDAC and characterized the landscape of the PDAC TME using multiple spatial molecular profiling technologies[8-18]. While these studies have provided insights into immune dysfunction, CAF subtype heterogeneity, and desmoplastic remodeling, they have primarily focused on global tissue-level patterns or pre-selected regions (i.e. juxtatumoral vs. panstromal). Furthermore, the complex cellular interactions between CAFs, immune cells, and tumor cells within PDAC malignant ductal regions remain unknown. These ducts are the sites of tumor origin, progression, and metastasis that shape the global PDAC TME and its consequent biology, making the study of cellular colocalization and signaling in these sites critical to understand PDAC carcinogenesis[19-22]. Since these ductal regions represent the critical interface between malignant epithelium and infiltrating immune cells, defining the stromal barriers that restrict immune access in these regions is crucial for understanding and overcoming immune exclusion in PDAC.

Here, we identified periductal CAF density in malignant ducts within invasive PDAC as a key tumor organizational feature that dictates immune access to tumor epithelium. Using complementary spatial approaches, including imaging mass cytometry (IMC) and multiplex immunohistochemistry (mIHC), in separate cohorts of PDAC samples, we mapped periductal cellular interactions and found that periductal fibroblast organization is the principal determinant of leukocyte infiltration in malignant ductal regions. Increased periductal fibrosis correlated with increased collagen I deposition and increased proliferation of epithelial cells and corresponded with reduced leukocyte-epithelial proximity, particularly with regards to natural killer (NK) cells. Ligand-receptor inference analysis of a recently published scRNA-seq dataset[23] of PDAC samples from 16 patients revealed increased collagen signaling from CAFs to leukocytes via CD44, and CD44 neutralization *in vitro* increased NK cell motility through the ECM. These results indicate that (1) periductal CAF architecture governs leukocyte access while promoting malignant epithelial cell proliferation and (2) targeting stromal checkpoints, such as CD44, may improve leukocyte infiltration and overcome ECM-mediated immune exclusion. Collectively, CAF-stratified ductal spatial architecture defines a new framework for analyzing PDAC fibrotic restrictions to leukocyte infiltration that can potentially be overcome through neutralization of stromal checkpoints in PDAC and other highly fibrotic tumors.

97 **Results**

98 **Fibroblast composition organizes spatial architectures that determine immune access to**
99 **malignant epithelial ducts in PDAC**

100 We first performed IMC on a tissue microarray (TMA) of primary tumor samples from
101 21 treatment-naïve PDAC patients to define the major cellular compartments of the tumor
102 microenvironment (TME). IMC is a high-dimensional spatial proteomics platform that maintains
103 tissue architecture while capturing single-cell protein levels[24]. We used a custom 40-marker
104 metal-conjugated antibody panel targeting cells from epithelial, immune and stromal lineages
105 (**Supplementary Table S1).** Following imaging and cell segmentation, we identified 412,862
106 cells in 44 IMC pseudoimages, with two or more primary tumor cores being imaged for some
107 patient **(Supplementary Table S2)**. Using a Seurat-based analysis pipeline[25-29], single-cell
108 protein expression data were log-normalized, and cell populations were identified using
109 clustering approaches[30], which resolved eight principal cell types encompassing malignant
110 epithelial cells, cancer-associated fibroblasts (CAFs), leukocytes, and other stromal populations
111 (**Supplementary Fig. S1**). Subclustering distinguished functional states: active, proliferative, or
112 inhibitory, within each lineage (**Supplementary Fig. S2**). This cellular map established the
113 framework for subsequent analyses of how CAF organization around malignant ducts constrains
114 leukocyte access within the PDAC TME.

115 Having defined major cellular lineages by IMC, we next examined how these populations
116 are spatially organized within the PDAC TME. Using cellular neighborhood analysis[31], we
117 classified distinct multi-cellular structures based on their cellular composition and proximity[31].
118 This analysis identified eight distinct cellular neighborhoods (**Figs. 1A-B**) each defined by

119 characteristic combinations of epithelial, fibroblast, and immune populations. Fibroblast
120 composition influenced neighborhood architecture: FAP^+ fibroblast-rich regions (neighborhood
121 6) were associated with proliferative epithelial areas, while αSMA^+ fibroblast-rich regions
122 (neighborhood 7) were enriched for $CD4^+/CD8^+$ T cells and macrophages (**Fig. 1C**). In contrast,
123 immune-enriched neighborhood 4 showed the majority of apoptotic epithelial cells and was
124 largely depleted of FAP^+ or αSMA^+ fibroblasts, consistent with reduced stromal barriers in
125 immune-accessible regions (**Fig. 1C, Supplementary Fig. S3)**. Notably, neighborhood 2 was
126 enriched for $IFN\gamma^+$ positive epithelial cells, a marker of immune activation[32] (**Fig. 1C,**
127 **Supplementary Fig. S3**). These epithelial neighborhoods also contained a higher density of
128 leukocytes relative to fibroblasts (**Supplementary Fig. S3)**, supporting that immune cell
129 accumulation occurs preferentially in epithelial compartments with reduced stromal architecture.
130 Consistent with previous reports in untreated PDAC[11], adaptive lymphoid cells ($CD4^+/CD8^+$ T
131 cells, B cells) were confined to their own distinct neighborhood (3) and were spatially segregated
132 from epithelial rich regions (**Fig. 1C**). In contrast, activated NK cells, based on Granzyme B
133 expression, were observed in epithelial-dominant neighborhoods (1, 2, 6, and 8), suggesting that
134 innate immune cells mediate the primary immune interactions at malignant ducts.
135 Although CAF-mediated immune exclusion has been reported in PDAC[9, 16], our analysis
136 defines how distinct fibroblast subsets establish reproducible spatial architectures that dictate the
137 degree of immune access to malignant ducts**.** Epithelial dominant neighborhoods (1, 2, 6, and 8)
138 displayed variable leukocyte abundance depending on surrounding fibroblast density (**Fig. 1C**).
139 Collectively, these analyses reveal that immune accessibility in PDAC is determined not by total
140 stromal content, but by the local fibroblast organization encasing malignant epithelial ducts,

141 prompting a focused analysis of epithelial-ductal regions to quantify how fibroblast abundance
142 constrains leukocyte access within the TME.

143 Given that neighborhood analysis captures higher-order organization but not direct
144 cellular interactions, we next applied a permutation-based interaction analysis[28], which identifies
145 significant deviations from a random cellular arrangement, to infer colocalization between
146 PDAC cellular subsets identified via IMC. Specifically, this analysis reveals which cellular
147 subsets are spatially interacting more or less frequently than expected due to random variation.
148 As expected, epithelial cells, fibroblasts, and immune cells tended to localize with cells of the
149 same type (**Fig. 1D**). Confirming neighborhood analysis, activated NK cells, but not T cells,
150 frequently interacted with apoptotic epithelial cells (**Fig. 1D)** while activated $CD4^+$ and $CD8^+$ T
151 cells primarily associated with one another rather than with epithelial or stromal cells (**Fig. 1D**).
152 Macrophages, on the other hand, most often interacted with αSMA^+ fibroblasts (**Fig. 1D**).

153 To visualize these multicellular relationships within the TME, we performed a cell–cell
154 network analysis defined from the average distance of spatial neighbors[33], which shows that
155 macrophage and αSMA^+ fibroblast nodes have the closest cross-lineage connectivity, whereas
156 NK cell nodes clustered near epithelial cell nodes, distinct from $CD4^+/CD8^+$ T cell and B cell
157 networks (**Fig. 1E**). This network structure suggest that fibroblast organization not only
158 structures epithelial–stromal interfaces but also constrains immune cell localization within the
159 PDAC TME.

160 Validation in an independent cohort of PDAC tumors (n = 17) using multiplex
161 immunohistochemistry (mIHC) confirmed the spatial relationships observed by IMC
162 (**Supplementary Fig. S4A**). Fibroblasts and epithelial cells constituted the majority of the
163 PDAC TME (**Supplementary Fig. S4B**). Notably, αSMA^+ fibroblast content was inversely

164 correlated with NK cell, but not macrophage, abundance (**Supplementary Fig. S4C**). $CD16^+$ NK
165 cells and macrophages, consistent with a pro-inflammatory phenotype[34, 35], were reduced with
166 higher αSMA^+ fibroblast content in tumors, supporting cell-cell network analysis and suggesting
167 a selective exclusion of effector leukocytes in fibroblast-rich regions (**Fig. 1E**). Overall, these
168 analyses demonstrate that fibroblast organization determines immune architecture in PDAC,
169 limiting the spatial access of pro-inflammatory, cytotoxic leukocytes to malignant epithelial
170 ducts.

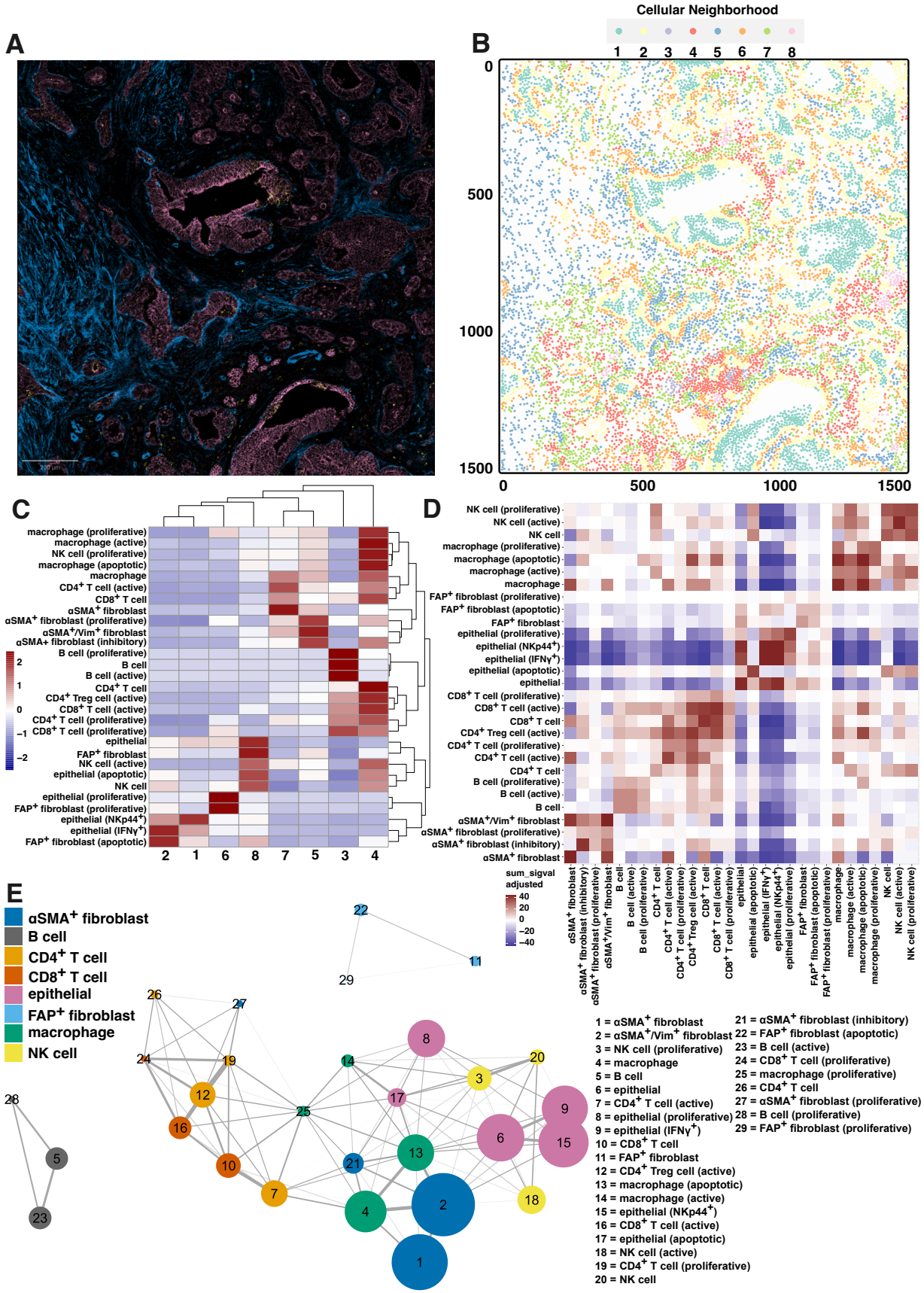
A
B
Cellular Neighborhood
1 2 3 4 5 6 7 8
0
500
1000
1500
C
macrophage (proliferative)
macrophage (active)
NK cell (proliferative)
macrophage (apoptotic)
macrophage
CD4+ T cell (active)
CD8+ T cell
αSMA+ fibroblast
αSMA+ fibroblast (proliferative)
αSMA+/Vim+ fibroblast
αSMA+ fibroblast (inhibitory)
B cell (proliferative)
B cell
B cell (active)
CD4+ T cell
CD4+ Treg cell (active)
CD8+ T cell (active)
CD4+ T cell (proliferative)
CD8+ T cell (proliferative)
epithelial
FAP+ fibroblast
NK cell (active)
epithelial (apoptotic)
NK cell
epithelial (proliferative)
FAP+ fibroblast (proliferative)
epithelial (NKp44+)
epithelial (IFNγ+)
FAP+ fibroblast (apoptotic)
2 1 6 8 7 5 3 4
D
sum_sigval adjusted
E
αSMA+ fibroblast
B cell
CD4+ T cell
CD8+ T cell
epithelial
FAP+ fibroblast
macrophage
NK cell
1 = αSMA+ fibroblast
2 = αSMA+/Vim+ fibroblast
3 = NK cell (proliferative)
4 = macrophage
5 = B cell
6 = epithelial
7 = CD4+ T cell (active)
8 = epithelial (proliferative)
9 = epithelial (IFNγ+)
10 = CD8+ T cell
11 = FAP+ fibroblast
12 = CD4+ Treg cell (active)
13 = macrophage (apoptotic)
14 = macrophage (active)
15 = epithelial (NKp44+)
16 = CD8+ T cell (active)
17 = epithelial (apoptotic)
18 = NK cell (active)
19 = CD4+ T cell (proliferative)
20 = NK cell
21 = αSMA+ fibroblast (inhibitory)
22 = FAP+ fibroblast (apoptotic)
23 = B cell (active)
24 = CD8+ T cell (proliferative)
25 = macrophage (proliferative)
26 = CD4+ T cell
27 = αSMA+ fibroblast (proliferative)
28 = B cell (proliferative)
29 = FAP+ fibroblast (proliferative)

171

172 **Figure 1: Fibroblast composition organizes spatial architectures that determine immune**
173 **access to malignant epithelial ducts in PDAC. A.** Corresponding patient IMC pseudoimage for
174 CN spatial plot in **B** (αSMA = blue; E-cadherin, Pan-cytokeratin = pink; NKG2D = yellow, scale
175 bar = 200 μm). **B.** Representative spatial plot of CNs in the human PDAC TME (CN1 = teal,
176 CN2 = yellow, CN3 = purple, CN4 = red, CN5 = blue, CN6 = orange, CN7 = lime, CN8 = pink).
177 **C.** Cellular neighborhood (CN) analysis revealed 8 distinct cellular neighborhoods (y-axis:
178 cellular neighborhoods; red = high proportion of cell subpopulation of interest (x-axis) within
179 cellular neighborhoods, blue = low proportion of cell subpopulation of interest within cellular
180 neighborhoods). **C. D.** Cellular interaction analysis (blue = strong avoidance, red = strong
181 interaction; FDR, $p < 0.01$) of IMC-defined cell subpopulations. **E.** Network graph of the top
182 75% of interactions between all IMC-defined cell populations in human PDAC showing
183 epithelial cells and NK cells exist in similar networks.
184
185 **CAF-stratified ductal spatial architecture governs immune access in PDAC**
186 Given that increased αSMA^+ fibroblasts are inversely correlated with effector leukocyte
187 infiltration (**Supplementary Fig. S4C**), we next sought to understand how per-ductal fibroblasts
188 influence leukocyte infiltration in regions near the duct. Using epithelial-ductal regions of
189 interest (ROIs) defined from IMC-based cellular neighborhood analysis, we applied Seurat's[27]
190 CellSelector function to isolate and quantify immune and stromal populations across 952
191 epithelial-ductal ROIs. These ROIs were stratified into 4 quartiles (Q1-Q4) according to
192 fibroblast abundance, with Q1 representing fibroblast-low and Q4 representing fibroblast-high
193 ducts. This stratification revealed a consistent CAF-stratified ductal spatial architecture (**Figs.**
194 **2A-B**) where increasing fibroblast content corresponded to progressive restriction of leukocyte–

195 epithelial proximity. Fibroblast abundance increased significantly across quartiles (**Fig. 2C**),
196 driven predominantly by αSMA$^+$ fibroblasts, rather than FAP$^+$ fibroblasts (**Supplementary Fig.**
197 **S5**), supporting previous reports that αSMA$^+$ fibroblasts cluster in periglandular regions[36]. As
198 expected, increasing fibroblast abundance was associated with a corresponding rise in Collagen I
199 expression (**Fig. 2D**), consistent with fibroblast-driven matrix deposition[37]. While total epithelial
200 cells decreased with increasing fibroblast content (**Fig. 2E**), proliferative epithelial cells
201 increased (**Fig. 2E**), supporting the interpretation that periductal fibroblast infiltration supports
202 epithelial cell growth.

203 We next assessed the impact of fibroblasts on the spatial associations of activated
204 leukocytes with ductal epithelial cells. Expression of NKG2D, an activating receptor expressed
205 on human lymphocytes[38], declined as fibroblast and collagen content increased (**Fig. 2B**).
206 Among immune subsets, NK cells showed the strongest sensitivity to fibroblast density; their
207 abundance was highest in fibroblast-low ducts (Q1) and decreased progressively across quartiles
208 (**Fig. 2F**), indicating fibroblast-dependent exclusion of cytotoxic innate lymphocytes. In contrast,
209 CD4$^+$ and CD8$^+$ T cell levels remained relatively stable (**Fig. 2F**), consistent with their
210 preferential localization to stromal rather than malignant ductal epithelium[39]. The loss of NK cell
211 infiltration was accompanied by reduced IFNγ$^+$ epithelial cells (**Supplementary Fig. S6E**),
212 implicating diminished NK-epithelial cell interactions and associated cytolytic signaling. In
213 fibroblasts-sparse ducts(Q1-Q2) , NK cells retained high expression of activation markers
214 (CD69, CD107a, IFNγ) (**Supplementary Fig. S7**), and displayed significant increases in
215 Granzyme B expression (**Fig. 2G**), confirming preserved effector function where malignant
216 epithelial cell access is maintained.

Collectively, these findings establish CAF-stratified ductal spatial architecture as a defining architecture feature of PDAC, whereby periductal fibroblast density promotes malignant epithelial proliferation while restricting NK cell infiltration and activation. This represents a novel mechanism of immune evasion in PDAC and suggests that periductal stromal remodeling to reduce fibroblast density or collagen deposition may be required to enable effective lymphocyte-based immunotherapies.

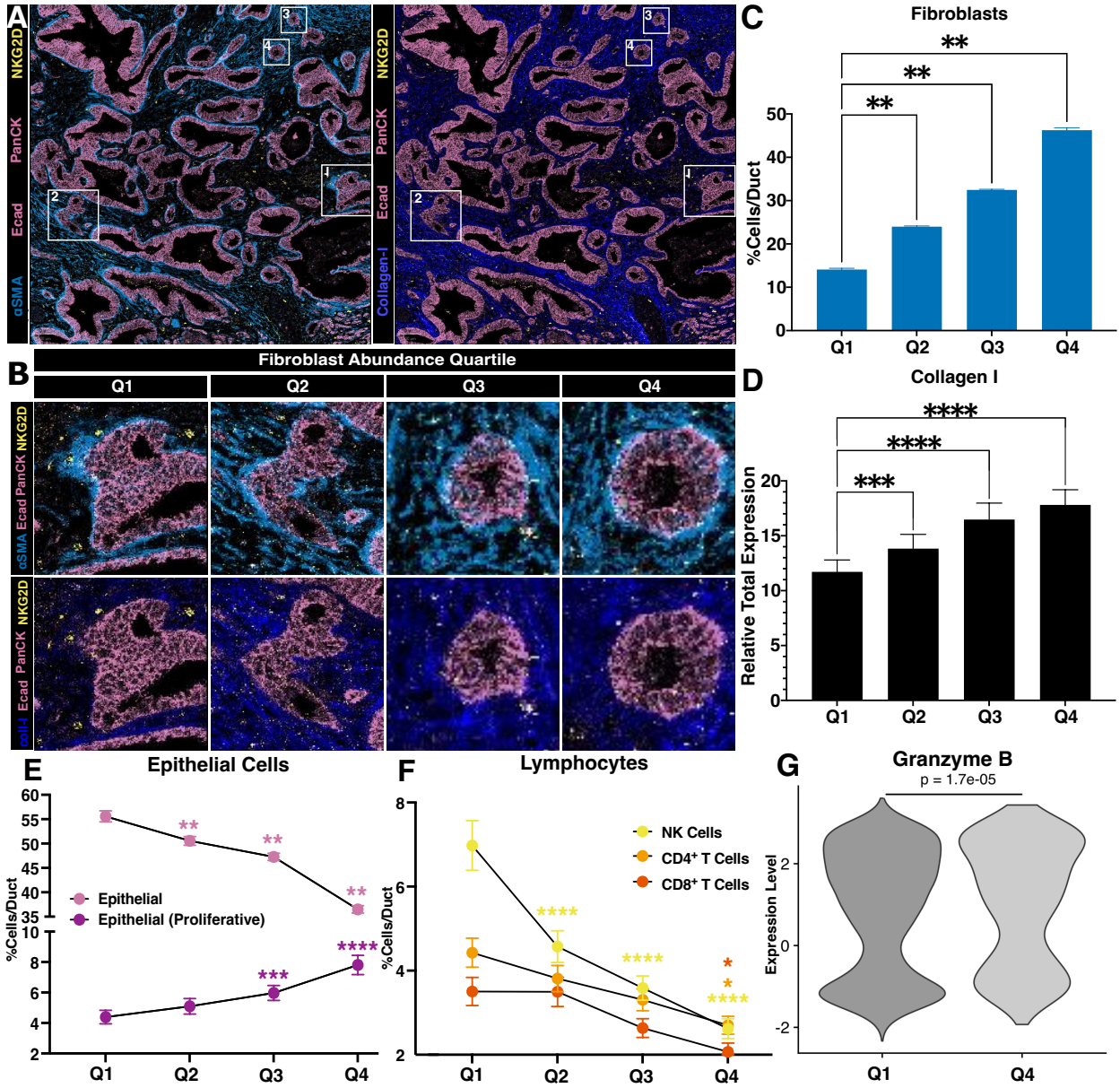

224 **Figure 2: CAF-stratified ductal spatial architecture govern immune access in PDAC.**
225 **A.** Representative IMC pseudoimages showing αSMA (left, light blue) or collagen-I (right, dark
226 blue) with pan-cytokeratin (panCK, pink), E-cadherin (Ecad, pink), and NKG2D (yellow); scale
227 bar = 100 μm with white boxes of each fibroblast abundance quartile with corresponding
228 numbers. **B.** Insets of representative epithelial-ductal ROIs from each fibroblast abundance
229 quartile (Q1=238, Q2= 235, Q3=240, Q4=239) shown in the white insets in **A**. **C.** Bar plot of
230 percent cells/ducts (mean ± SEM) of total fibroblasts, **D.** Bar plot of percent cells/ducts (mean ±
231 SEM) of total collagen-I expression in epithelial-ductal ROIs ranked by fibroblast abundance
232 quartile (2-way ANOVA; *$p < 0.05$, ** $p < 0.01$, ***$p < 0.001$, ****$p < 0.0001$; Q1=55, Q2=
233 58, Q3=57, Q4=60). **E**. Connecting line plot of percent cells/ducts (mean ± SEM) of total
234 epithelial cells and proliferative epithelial cells (2-way ANOVA; *$p < 0.05$, ****$p < 0.0001$; all
235 quartiles compared to Q1). **F.** Connecting line plot of percent cells/ducts (mean ± SEM) of NK
236 cells, $CD4^+$ T Cells, and $CD8^+$ T Cells (2-way ANOVA; *$p < 0.05$, ****$p < 0.0001$; all quartiles
237 compared to Q1). **G.** Violin plot showing NK cell-based expression in Q1 and Q4 fibroblast
238 abundance quartiles of Granzyme B (Kruskal-Wallis test).
239
240 **Cell-cell communication analysis implicates CD44 as a stromal checkpoint mediating NK-**
241 **ECM interactions**
242 Because NK cell access to malignant ducts was inversely correlated with periductal
243 fibroblast density (**Fig. 2F–G**), we next sought to identify the molecular pathways that could
244 mediate these fibroblast-NK cell interactions within the PDAC tumor microenvironment. We
245 applied ligand-receptor inference of cell to cell communication with CellChat[40] to a reference
246 immune-enriched human PDAC scRNAseq dataset containing matched adjacent-normal

247 (AdjNorm) and PDAC tumor samples[23]. To distinguish malignant from normal epithelial cells,
248 we used CytoTRACE to infer differentiation states[41,42]. We also subclustered fibroblasts to
249 resolve canonical CAF subsets, including myofibroblasts (myCAFs; *FAP, MMP11, HOPX,*
250 *POSTN, COL12A1*)[9], inflammatory (iCAFs; *CFD, DPT, AGTR1, CXCL12, CCL2*)[9], antigen-
251 presenting (apCAFs; *HLA-DRA, HLA-DPA1, HLA-DQA1*)[9], normal fibroblasts, and stellate-like
252 fibroblasts (*MYH11, RGS5)*[43, 44] (**Supplementary Figs. S8A-E**).
253 Because NK cells were the immune population most affected by periductal fibroblast
254 density (**Fig. 2G–H**), we next examined whether fibroblasts engage in molecular signaling that
255 could underlie this selective exclusion. CellChat analysis revealed that CAFs in PDAC,
256 particularly iCAFs and myCAFs, exhibited increased outgoing signaling compared with
257 adjacent-normal fibroblasts, whereas NK cells and malignant epithelial cells served as prominent
258 signal receivers (**Fig. 3A-B**). This suggests that CAF-derived signaling networks may directly
259 modulate NK cell behavior and epithelial interactions, extending their role beyond structural
260 confinement.
261 Among enriched signaling pathways, collagen signaling showed the largest PDAC-
262 specific increase, driven by upregulation of multiple collagen isoforms (**Fig. 3C**). Within this
263 network, NK cells were predicted to receive collagen-derived signals through CD44 (**Fig. 3D**), a
264 principal receptor mediating cell–matrix adhesion on leukocytes[45]. Differential expression
265 analysis confirmed upregulated CD44 expression in NK cells within the PDAC TME, concurrent
266 with transcriptional upregulation of collagen genes in malignant epithelial cells, iCAFs, and
267 myCAFs (**Fig. 3D, Supplementary Fig. S9**).
268 Together, these findings implicate the collagen–CD44 axis as a critical CAF-to-NK
269 communication route that reinforces stromal confinement of cytotoxic lymphocytes. This

represents a stromal checkpoint mechanism in which NK cells are sequestered within collagen-rich regions. We hypothesize that this CAF-NK cell signaling pathway limits the migration of NK cells toward tumor targets. Hence, disrupting CD44–collagen interactions could restore NK-cell motility and enhance antitumor function in PDAC.

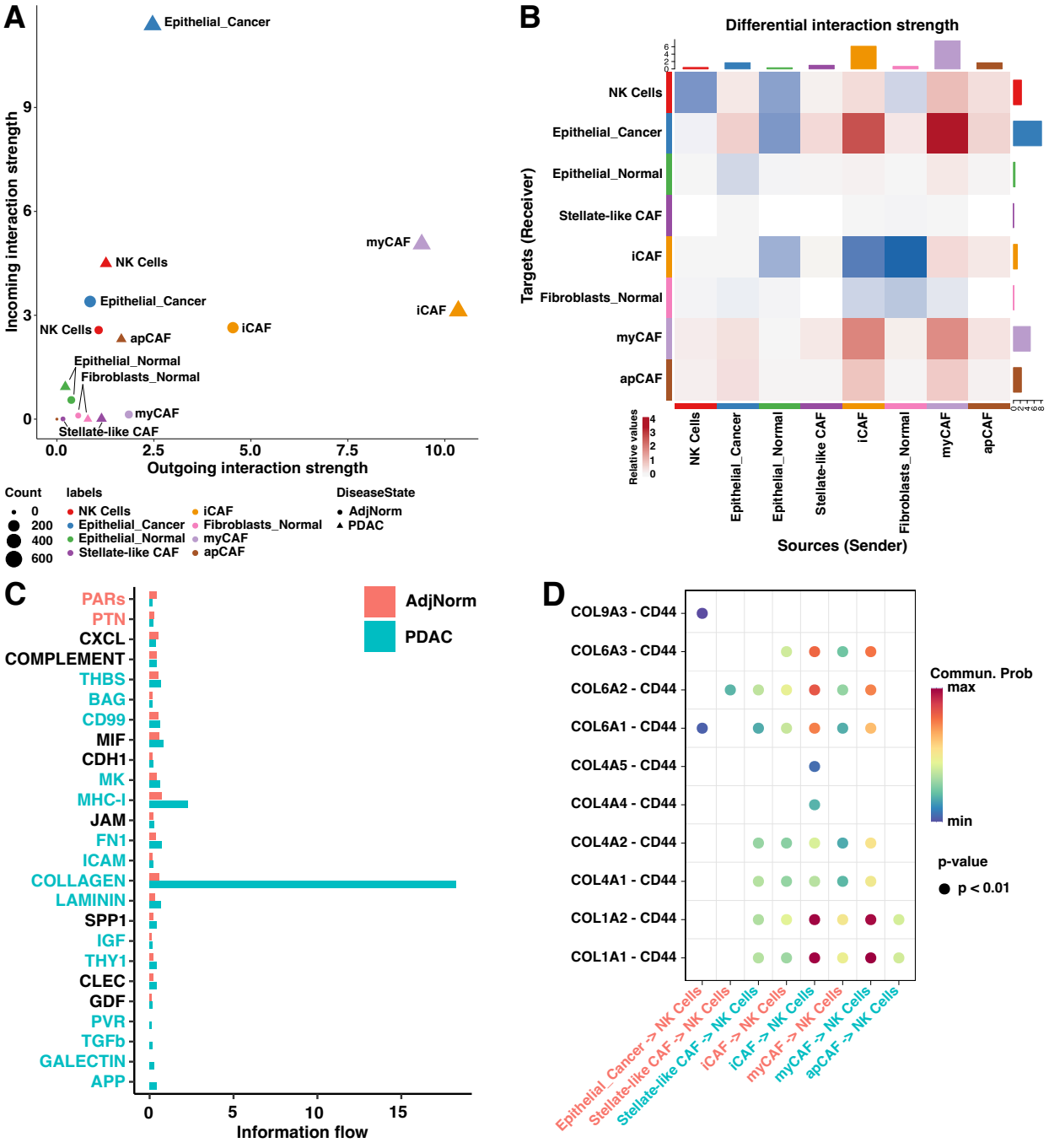

275 **Figure 3: Cell-cell communication analysis implicates CD44a stromal checkpoint mediating**
276 **NK- ECM interactions. A.** Incoming and outgoing interaction strength for each cell population
277 grouped by AdjNorm and PDAC disease states. **B.** Heatmap of differential interaction strengths
278 of target (y-axis) and source (x-axis) cells with bar plots displaying the absolute values of
279 interactions. **C.** Communication probabilities of signaling pathways targeting NK cells between
280 AdjNorm and PDAC disease states as measured by information flow (pathway legend: pink =
281 AdjNorm-specific, teal = PDAC-specific, black = equally specific). **D.** Significant ligand-
282 receptor pairs from the COLLAGEN signaling pathways targeting NK cells upregulated in
283 PDAC compared to AdjNorm (interaction legend (x-axis): pink = AdjNorm, teal = PDAC).
284

285 **CD44 blockade enhances NK cell invasion *in vitro***

286 Given that NK cells in the PDAC TME primarily engage the collagen pathway through
287 CD44 (**Figs. 3C-D**), we hypothesized that CD44-mediated interactions with ECM components
288 physically restrict NK cell infiltration by anchoring them within the stroma. To test this, we first
289 confirmed CD44 expression on human donor NK cells by flow cytometry (**Supplementary Fig.**
290 **S10**). We then evaluated NK cell invasion through basement-membrane and collagen-containing
291 matrices *in vitro.* In a 2D Transwell assay, membranes were coated with Matrigel (rich in ECM
292 components[46]), and NK cells were incubated with or without a CD44-neutralizing antibody (α-
293 CD44) (**Fig. 4A**). CD44 blockade significantly enhanced NK cell invasion in three of four
294 human donor NK cell samples (**Figs. 4B-E**).

295 To validate these findings in a more physiological context, we employed a 3D *in vitro*
296 model using a collagen-rich tumor spheroid assay (**Fig. 4F**). Human PANC-1 spheroids were
297 embedded with donor NK cells in a Collagen I–Matrigel matrix and cultured for 24 hours with or

298 without α-CD44. Immunofluorescence imaging showed increased NK-cell penetration into
299 PANC-1 spheroids upon CD44 blockade across three donor NK cells (**Figs. 4G-K**,
300 **Supplementary Fig. S11**). To determine whether this enhanced invasion involved CD44-
301 dependent modulation of extracellular matrix degradation[47, 48], we analyzed matrix
302 metalloproteinase (MMP) gene expression in human donor NK cells treated with or without α-
303 CD44 for 1 or 4 hours[47, 48]. No significant differences were observed (**Supplementary Fig. S12,**
304 **Supplementary Table S5**), strongly suggesting that CD44 neutralization facilitates NK cell
305 invasion primarily by disrupting adhesion to collagen, rather than altering proteolytic activity.
306 Together, these results demonstrate that CD44 functions as an inhibitory anchor for NK
307 cells within the collagen-rich PDAC stroma. Blocking CD44–collagen binding restores NK-cell
308 mobility and invasive capacity, providing a mechanistic rationale for targeting stromal
309 checkpoints to enhance lymphocyte infiltration in desmoplastic tumors.

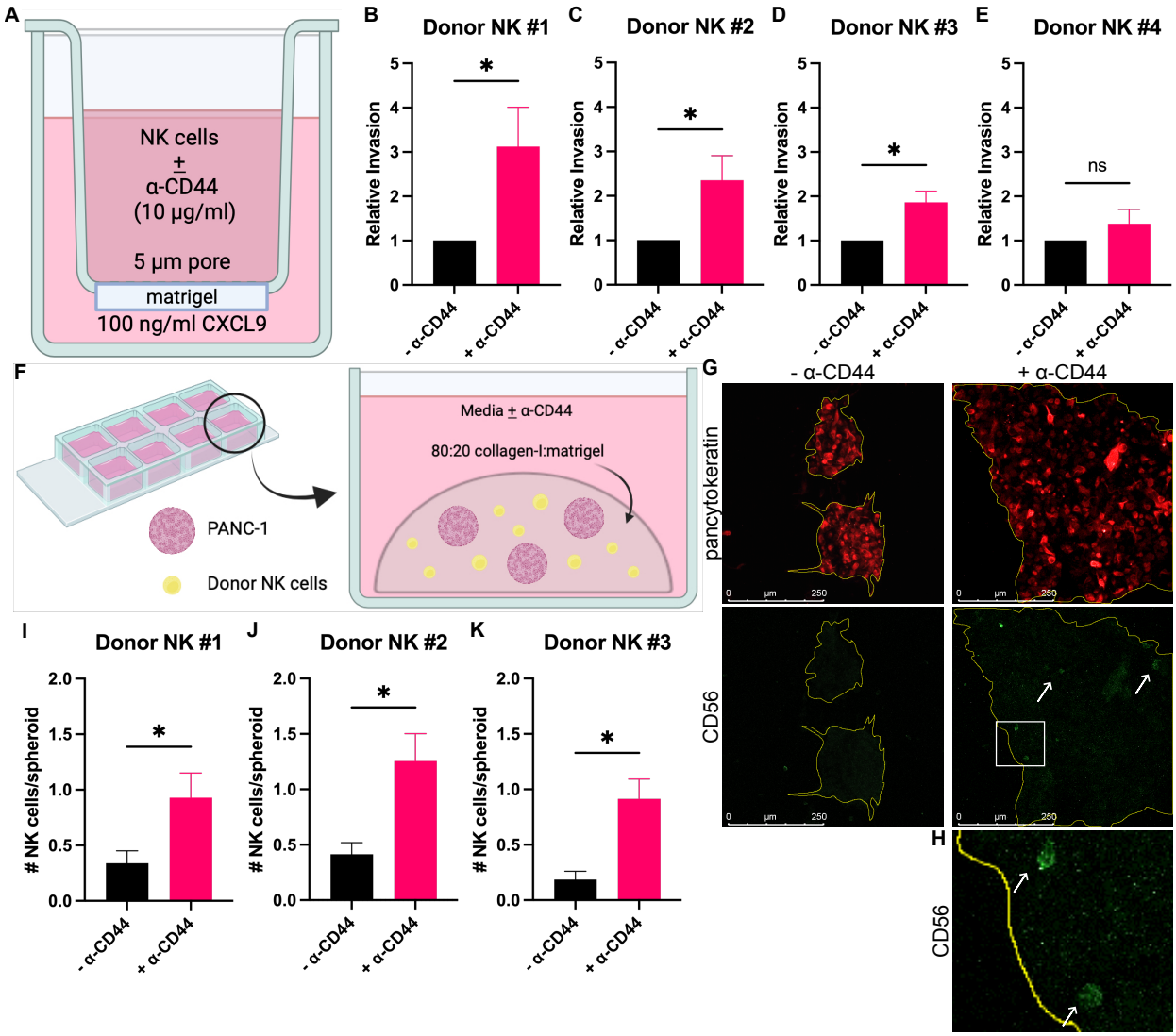

Figure 4: CD44 blockade enhances NK cell invasion *in vitro*. A. Schematic for Transwell invasion assays. Average relative invasion (± SEM) of **B.** Donor NK #1 (n = 9), **C.** Donor NK #2 (n = 12), **D.** Donor NK #3 (n = 6), and **E.** Donor NK #4 (n = 10) upon CD44 neutralization. *$p < 0.05$ as determined by Wilcoxon matched-pairs signed rank test. **F.** Schematic of spheroid invasion assay. **G.** Representative 20X IF images of outlined (yellow) PANC-1 spheroids (Pan-cytokeratin; red) embedded with NK cells (CD56; green), pointed out with white arrows, treated with or without α-CD44. Scale bar = 250 µm. **H.** Zoomed inset of NK cells in the α-CD44 treatment group in **G** (white box). Average number of NK cells per PANC-1 spheroid (± SEM)

319 from **I.** Donor NK #1 (- α-CD44, n = 53; + α-CD44, n = 42), **J.** Donor NK #2 (- α-CD44, n = 29;

320 + α-CD44, n = 43), and **K.** Donor NK #3 (- α-CD44, n = 27; + α-CD44, n = 47); n = # of

321 spheroids analyzed; *$p < 0.05$ as determined by Wilcoxon matched-pairs signed rank test.

322 **Discussion**

323 Recent reports characterizing immune-stromal interactions in PDAC using single-cell
324 technologies have characterized the stromal heterogeneity and impact of CAFs on the PDAC
325 TME[8-18]. However, the impact of stromal architecture on CAF, tumor cell, and leukocyte
326 interactions and leukocyte infiltration in malignant ductal regions, the critically important tumor-
327 immune interface, remains unexplored. Here, we define CAF-stratified ductal spatial architecture
328 as a key organizational feature of the PDAC TME that dictates leukocyte access to malignant
329 epithelium. Utilizing an approach that combines IMC, mIHC, and scRNA-seq to map periductal
330 cellular interactions, we have demonstrated that periductal fibroblast organization is a critical
331 determinant of leukocyte infiltration in malignant ductal regions. IMC and mIHC analyses
332 collectively revealed that fibroblast abundance inversely correlated with immune accessibility,
333 with NK cells being the leukocyte subset most sensitive to fibrous density. These data establish
334 periductal fibroblast composition, not total fibrosis, as the dominant structural determinant of
335 immune exclusion in PDAC.

336 Cell-to-cell communication analysis revealed that CAFs function as the dominant senders
337 of signals within the PDAC TME, engaging both epithelial and NK cells through collagen-
338 mediated pathways. The collagen-CD44 axis emerged as the principal CAF-to-NK signaling
339 pathway, positioning CD44 as a stromal checkpoint that restricts leukocyte motility and
340 reinforces fibroblast-mediated immune exclusion at malignant ducts. Functionally, CD44
341 blockade restored NK cell infiltration through collagen-rich matrices without altering MMP
342 expression, indicating that neutralizing CD44–collagen adhesion, not ECM degradation,
343 overcomes such barriers.

344 In PDAC, stromal elements, including CAF-derived chemokines (e.g., CXCL12)[49] and
345 ECM-derived ligands, such as fibronectin that engage inhibitory receptors like ILT3[50], have been
346 shown to modulate immune suppression within the TME. For example, elevated stromal
347 CXCL12 correlates with the exclusion of cytotoxic T cells from tumor nests, while fibronectin
348 engagement of the inhibitory receptor ILT3 on intra-tumoral myeloid cells induces a suppressive
349 phenotype, collectively demonstrating that stromal components can directly regulate immune
350 positioning and activation. Together, these findings indicate that the desmoplastic stroma
351 functions not only as a physical barrier but also as an active regulatory element, acting as a
352 "stromal checkpoint," in which CAF-derived and ECM-mediated signals restrict leukocyte
353 access and engagement with malignant epithelial cells. Our data extend this framework by
354 identifying impaired immune trafficking as a key regulatory mechanism mediated through
355 CD44–ECM interactions. Given that broad stromal ablation and ECM degradation have proven
356 unsuccessful in restoring intra-tumoral leukocyte functionality or limiting tumor growth
357 preclinically and clinically[51, 52], our data highlight the potential of instead targeting stromal
358 checkpoints, such as CD44, to enhance NK cell motility and infiltration, thus improving the
359 efficacy of NK cell-dependent immunotherapies in PDAC.
360 In summary, our findings establish fibroblast composition as a central determinant of
361 PDAC tissue architecture and immune accessibility. Focusing on malignant ductal regions, we
362 define CAF-stratified ductal spatial architecture as the structural basis of immune exclusion and
363 identify CD44 as a molecular mediator of this stromal checkpoint. High-CAF ducts promote
364 epithelial cell proliferation while restricting lymphocyte access, particularly NK cells, whereas
365 low-CAF ducts preserve effector function and cytolytic ability. Thus, targeting stromal
366 checkpoints, in combination with immunotherapy and KRAS inhibitors, presents an opportunity

367 to increase leukocyte infiltration irrespective of ECM degradation in PDAC and other solid

368 tumors.

369

370 **Methods**

371 **Tissue samples, antibody validation, metal-conjugation, and imaging mass cytometry**
372 **(IMC)**

373 The Lombardi Comprehensive Cancer Center (LCCC) Histopathology & Tissue Shared
374 Resource (HTSR) provided formalin-fixed, paraffin-embedded (FFPE) human PDAC and spleen
375 tissue samples. For IMC, we used a LCCC-curated FFPE human pancreas tissue microarray
376 (TMA) slide series containing 2 mm cores from normal pancreas, pancreatitis, pancreatic
377 neuroendocrine tumors, intraductal papillary mucinous neoplasm, pancreatic mucinous
378 adenocarcinoma, PDAC, colon adenocarcinoma, testicle, tonsil, and placenta samples, and
379 PDAC cell lines. Information for all TMA samples are available at doi:
380 10.5281/zenodo.10582038. The IMC study was restricted to 44 cores from 21 previously
381 untreated PDAC patients who underwent Whipple resections or distal pancreatectomies
382 (**Supplementary Table S2**).

383 For IMC, we designed a metal-conjugated antibody panel. Carrier-free antibodies not
384 commercially metal-conjugated were validated by IF in PDAC or spleen tissue (**Supplementary**
385 **Table S1**). Antibodies with expected expression patterns were metal-conjugated using MaxPar
386 X8 Multimetal Labeling Kits (Standard Bio Tools (SBI); (**Supplementary Table S1**). Metal-
387 conjugation was validated by cytometry by time-of-flight (CyTOF) (Hyperion Imaging System;
388 SBI) at the LCCC Flow Cytometry Shared Resource (FCSR). Metal-conjugated antibody
389 dilutions were optimized in the pancreas TMA prior to final IMC staining at the HTSR. Antigen
390 retrieval and staining was performed (SBI) at the LCCC HTSR, while image acquisition was
391 performed at the LCCC Mass Spectrometry and Analytical Pharmacology Shared Resource. A
392 maximum of 2.25 mm^2 regions of interest (ROIs) on TMA cores were selected, laser-ablated and

393 analyzed by CyTOF to quantitate the metal-conjugated antibodies per ROI, generating multiplex
394 images[53]. All data were collected using the Hyperion Imaging System (SBI) and qualitatively
395 validated in MCD Viewer (v1.0.560.6; SBI) and QuPath softwares (RRID:SCR_018257).
396

397 **IMC image processing, data transformation, and single-cell clustering**

398 Raw IMC data was processed following the widely used ImcSegmentationPipeline[54]
399 (https://github.com/BodenmillerGroup/ImcSegmentationPipeline). In the Ilastik software
400 (RRID:SCR_015246), DNA, E-cadherin, pan-cytokeratin, vimentin, and CD45RO markers were
401 used to pixel-train and generate cell segmentation probability maps for nuclear, cytoplasmic, cell
402 membrane, and background areas in all IMC images, which were imported into CellProfiler to
403 generate cell segmentation masks to then extract single-cell protein expression data using
404 histoCAT[28]. 412,862 cells were identified across 44 images from 21 PDAC patient samples.
405 Extracted IMC-derived single cell data were imported into R (v4.2.1) for downstream
406 computational analyses. histoCAT-derived single cell data files generated are available at doi:
407 10.5281/zenodo.10582038. All scripts adapted from this pipeline for downstream analyses are
408 available at https://github.com/Weiner-Lab/NaturalKillerCells_PDAC. Single cell protein
409 expression data was log-transformed, re-integrated, and clustered using Seurat-based analysis[27].
410 As single cell expression may contain "lateral spillover" into neighboring single cells as a result
411 of cell segmentation[54], we therefore used a supervised clustering approach to phenotype cells
412 based on canonical cellular morphology markers (αSMA, CD3, CD4, CD8α, CD11b, CD16,
413 CD20, CD45RO, CD56, CD68, E-cadherin, FAP, FOXP3, NKG2D, NKp44, pan-cytokeratin,
414 vimentin), we found that a clustering resolution = 0.35 provided distinct immune, fibroblast, and
415 epithelial cell populations. Each cell population was subsetted and re-clustered to identify the

416 functional state of subclusters using the following markers: CD69, CD107α, cleaved-caspase 3,
417 collagen-I, granzyme B, HLA-A/B/C, HLA-A1, IFNγ, Ki67, MICA, PCNA, perforin, PD-1, PD-
418 L1, and TGFβ. All cellular subclusters were reintegrated and annotated based on functional
419 classification: active subpopulations were solely immune cell based and were characterized by
420 high expression of known immune cell activation markers, CD69, CD107α, and/or IFNγ;
421 proliferative cell populations were characterized by high expression of proliferation markers
422 Ki67 and/or PCNA; and inhibitory subpopulations were characterized by high TGFβ expression,
423 which is known to be immune suppressive. Subclustering identified 29 unique cell populations,
424 which were validated visually using the Cytomapper R package and the MCD Viewer software.
425 Seurat objects containing all the PDAC single cell metadata is available at doi:
426 10.5281/zenodo.10582038 and were converted to SingleCellExperiment[54] objects for
427 downstream spatial analyses.
428
429 **IMC spatial analysis**
430 We generated knn-based interaction graphs for the 15-nearest neighbors and used k-
431 means clustering to group cells into 8 distinct cellular neighborhoods using the
432 SpatialExperiment and imcRtools R packages[54]. Using the imcRtools package, permutation test-
433 based cell-cell interaction analysis identified significant interactions or avoidances between cell
434 populations. Using FDR analysis, cell-cell interactions with $p < 0.01$ were considered
435 statistically significant. Based on Euclidean distance metadata, distance and network analyses
436 were performed, as previously described[33]. Seurat's CellSelector function[27] was used to select
437 and quantify cells in epithelial-ductal ROIs of spatial images. From CellSelector, percentages of
438 cell populations in each epithelial-ductal ROI were quantified, and epithelial-ductal ROIs were

439 stratified in quartiles based on fibroblast abundance (Q1 = low fibroblast quartile, Q4 = high
440 fibroblast quartile). Mean total expression of all markers was quantified in representative
441 epithelial-ductal ROIs of pseudoimages using MCD Viewer. Cell-based expression in epithelial-
442 ductal ROIs was performed using Seurat.
443
444 **Multiplex immunohistochemistry (mIHC)**
445 Sections of 5μm thickness were cut from FFPE tissue blocks containing PDAC tumor
446 samples. Patient samples were from 10 males and 7 females with age ranges between 45-88, and
447 had tumor diameters ranging from 0.1-8 cm (**Supplementary Table S3**). Samples were stained
448 for CD56, CD16, CD335, panCK, αSMA, and CD68 (**Supplementary Table S4**).
449 The slides were baked at 60°, deparaffinized in xylene, rehydrated, washed in distilled
450 water and incubated with 10% neutral buffered formalin (NBF) for an additional 20 minutes to
451 increase tissue-slide retention. Epitope retrieval/microwave treatment (MWT) for all antibodies
452 was performed by boiling slides in the respective Epitope Retrieval buffer (ER1, pH6 or ER2,
453 pH9; Leica Biosystems AR9961 or AR9640, respectively). Protein blocking was performed
454 using antibody diluent/blocking buffer (Akoya, ARD1001EA) for 10 minutes at room
455 temperature. Primary antibody/OPAL dye pairings, staining order and incubation conditions are
456 listed in the table below. The staining was performed using Leica Bond autostainer. Sections
457 were counterstained with spectral DAPI (Akoya FP1490) for 5 min and mounted with ProLong
458 Diamond Antifade (ThermoFisher, P36961) using StatLab #1 coverslips (CV102450). The order
459 of antibody staining and the antibody/OPAL pairing was predetermined using general guidelines
460 and the particular biology of the panel. General guidelines include spectrally separating co-
461 localizing markers and separating spectrally adjacent dyes. Multiplex IHC was optimized by

462 first performing single-plex IHC with the chosen antibody/OPAL dye pair to optimize signal
463 intensity values and proper cellular expression, followed by optimizing the full multiplex assay.
464 Slides were scanned at 10X magnification using the Phenoimager Fusion system Automated
465 Quantitative Pathology Imaging System (Akoya Biosciences). Whole slide scans were viewed
466 with Phenochart (Phenochart 2.2.0, Akoya) which also allows for the selection of high-powered
467 images at 20X (resolution of 0.5mm per pixel) for multispectral image capture. Multispectral
468 images of each tissue specimen were captured in their entirety.
469 Multiplex staining and imaging were performed as previously described[55], except tissue
470 images were captured using Akoya Biosciences Inc.'s PhenoImager Fusion imaging platform at
471 the LCCC HTSR. Images were exported as *.qptiff* files and visualized and processed using
472 QuPath software (RRID:SCR_018257).
473
474 **mIHC image processing and analysis**
475 mIHC images were processed using QuPath software (v0.6.0)[56]. Spectrally unmixed
476 images were visualized and a ROI grid, with each ROI measuring 500 µm via 500 µm, was
477 overlaid on each image. Cells within each ROI were then automatically segmented using the
478 StarDist machine-learning based pipeline[57], with the DAPI channel used to delineate nuclear
479 staining, normalized percentile set at (1, 99), threshold set at 0.5, and pixel size set at 0.5
480 µm/pixel. After cell segmentation, duplicate channel training images were created for each
481 marker to create an object classifier for each cell type. Under the direction of an experienced
482 pathologist, an object classifier was trained for each marker. This was repeated for three separate
483 images. Afterwards, object classifiers for each marker were then applied to each image for cell
484 phenotyping. Percentage of cells was calculated by dividing cells detected for marker of interest

485 by total cells in each ROI. All ROIs were then averaged to get a total value for each cell type of
486 interest for each image. Only ROIs with at least 500 cells were analyzed, with biologically
487 incompatible markers excluded from analysis.
488
489 **Single-cell RNA-sequencing analysis**
490 To infer ligand-receptor (L-R) interactions in PDAC, we utilized a previously published
491 human PDAC scRNAseq dataset[23] and subsetted NK cells, fibroblasts, and epithelial cells.
492 Malignant and normal epithelial cells were differentiated using CytoTRACE, a computational
493 framework that predicts cellular differentiation states by measuring the number of genes
494 expressed by each cell[41]. The CytoTRACE scores distribution was observed to be bi-modal and
495 using a mixed-model, an ideal cut-off value separating the two distributions was determined to
496 be 0.72 where scores greater than 0.72 indicated a malignant epithelial cells[58] (**Supplementary**
497 **Fig. S8**). Fibroblasts were subclustered into known subpopulations and we identified: antigen-
498 presenting CAFs (apCAFs), inflammatory CAF (iCAFs), myofibroblasts (myCAFs), normal
499 fibroblasts, and stellate-like fibroblasts[43] (**Supplementary Fig. S8**). We then used CellChat, a
500 manually curated protein database of approximately 2,000 L-R pairs[40] to infer potential L-R
501 interactions between epithelial, fibroblast, and NK cell populations. A Wilcox test with a
502 Bonferroni correction from the FindMarkers Seurat function (v4.3) was used for differential gene
503 expression analysis of CellChat-identified L-R genes. Genes with an adjusted-$P < 0.01$ were
504 considered significantly differentially expressed. R scripts for applied CytoTRACE and CellChat
505 analyses are available at https://github.com/Weiner-Lab/NaturalKillerCells_PDAC.
506
507

508 **Cell culture**

509 Human PANC-1 PDAC cells and donor NK cell lines were cultured, as previously
510 described[59, 60], except donor NK cells received 0.5% v/v of IL-2. Healthy human donor NK cell
511 lines, Donor NK #1, #2, and #4 were purchased (STEMCELL Technologies, Vancouver,
512 Canada), and Donor NK #3 cells were isolated from a leukoreduction system (LRS) chamber
513 (Inova Health System) and isolated via MojoSortTM Human NK Cell Isolation Kit (BioLegend,
514 CAT#: 480053). Donor NK cells were stimulated with the engineered K562 cell line
515 (RRID:CVCL_0004), K562-mb21-41BBL (courtesy of Dr. Dean Lee at Nationwide
516 Children's)[61]. K562-mb21-41BBL cells were cultured in supplemented RPMI (10% FBS, 1%
517 penicillin/streptomycin). For NK cell stimulation, K562-mb21-41BBL cells were collected (5
518 minutes, 1,000 rpm, 4˚C), resuspended in supplemented RPMI with mitomycin C (Sigma-
519 Aldrich) (C_f = 0.01 mg/ml) and incubated for 4 hours (37˚C). Pre-treated K562-mb21-41BBL
520 cells were collected (5 minutes, 1,000 rpm, 4˚C), resuspended in NK cell medium, then co-
521 cultured with donor NK cells (E:T = 1:1); this process was repeated at least once per week.
522 Donor NK cells aged day 1-50 and stimulated 1-3 days prior to *in vitro* assays were used. All cell
523 lines were tested and determined to be free of mycoplasma.

524

525 **Flow cytometry**

526 Cells were centrifuged (5 minutes, 1,000rpm, 4˚C) washed twice (1X PBS), then
527 resuspended in FACS staining buffer (1% BSA in 1X PBS). Human Fc block (BD Pharmigen,
528 CAT#: 564219) then α-CD44-BV605 (BioLegend, CAT#: 103047) antibodies were added per
529 manufacturer's recommendations (30 minutes, 4˚C). Cell pellets were washed twice (FACS
530 staining buffer), resuspended in fixative (1% PFA in 1X PBS), then processed by the LCCC

531 FCSR in a BD LSRFortessa Cell Analyzer (BD Biosciences). Analysis was performed using
532 FlowJo (v10.8.1; RRID:SCR_008520).
533
534 **NK cell 2D invasion assay**
535 The bottom of 5 µm Transwells (Corning) were coated with Matrigel (Corning) diluted
536 1:3 in NK cell medium. CXCL9 (C_f =100 ng/ml) (R&D Systems)-supplemented NK cell
537 medium was added to the bottom of each well. Donor NK cells were added to Transwells with or
538 without an α-CD44 neutralizing antibody (clone IM7; Bio X Cell; C_f = 10 µg/ml) and incubated
539 for 4 hours (37˚C). Transwells were removed, cells were stained with Trypan Blue Stain (Gibco)
540 and manually counted on a hemocytometer. Control cells were plated without Transwells to
541 count total cells to calculate percent invasion. Relative invasion is the percent of cells that
542 invaded through the transwell normalized to untreated NK cell conditions. A Wilcoxon matched-
543 pairs signed rank test was performed to determine statistical significance (GraphPad Prism v10;
544 RRID:SCR_002798).
545
546 **NK cell 3D spheroid invasion assay**
547 As previously described,[27] PANC-1 cells were seeded in each well of a low-adhesion U-
548 bottom plate, spun (5 minutes, 1,000 rpm, 4˚C) and cultured overnight. Spheroids were
549 embedded with donor NK cells in an 80:20 Collagen-I (Invitrogen): Matrigel (Corning) mixture
550 in chamber wells (Lab-Tek). Embedded spheroids were treated with α-CD44 (clone IM7; Bio X
551 Cell; C_f = 10 µg/ml) for 24 hours (37˚C) prior to immunocytochemistry (IC). For IC, samples
552 were fixed with 4% paraformaldehyde (PFA; 10 minutes, 25˚C), washed with 1X PBS (5
553 minutes), then permeabilized with 0.5% Triton-X100 (10 minutes). Cells were washed once,

554 blocked (1% BSA in 1X PBS, 30 minutes), then incubated with human Fc block (BD Pharmigen,
555 CAT#: 564219). Samples were incubated with pan-cytokeratin-eFluor™ 660 (Invitrogen, CAT#:
556 50-9003-82) and CD56 (Invitrogen, CAT#: MA1-19129) antibodies overnight (25˚C). An α-
557 Mouse IgG2a-AF488 secondary antibody (Invitrogen, CAT#: A-21131; 1-4 hours, 25˚C), cells
558 were washed 3 times, incubated with DAPI (50 ng/ml; 10 minutes, 25˚C), then washed twice.
559 Coverslips were mounted with anti-fade mountant, then and dried. Z-stacks of spheroids were
560 imaged using a Leica SP8 AOBS microscope at the LCCC Microscopy and Imaging Shared
561 Resource. Z-stacks were ≤ 1 µm. Z-stack images were processed and using FIJI software[62]
562 (v2.14.0; RRID:SCR_002285) for manual NK cell quantitation into PANC-1 spheroids.
563 Statistical significance was determined using a Wilcoxon matched-pairs signed rank test
564 (GraphPad Prism v10).
565
566 **Effects of CD44 neutralization on MMP gene expression in human NK cells**
567 Donor NK cell lines were incubated with or without α-CD44 (clone IM7; Bio X Cell; C_f
568 = 10 µg/ml) for 1 and 4 hours. Cells were collected (5 minutes, 1,000 rpm, 4˚C) and RNA was
569 isolated using the PureLink™ RNA Mini Kit (Ambion). RNA concentration was measured using
570 NanoDrop 8000 (ThermoFisher Scientific), then stored at -80˚C. Diluted RNA (20 ng/µl) was
571 treated with 10% v/v 10X DNase I Buffer and 10% v/v DNase I (Promega; 15 minutes, 25˚C).
572 10% v/v of RQ1 RNase/DNase Stop Solution (Promega) and 10% v/v Oligo(dT) nucleotides
573 (IDT) were added, then heat inactivated at 65˚C (10 minutes) then at 4˚C (5 minutes). cDNA was
574 synthesized with the GoScript™ Reverse Transcriptase Kit (Promega). qPCR was performed
575 using GoTaq qPCR Master Mix (Promega) with the StepOnePlus™ Real-Time PCR System
576 (ThermoFisher Scientific). Gene expression was quantified ($2^{-\Delta C_T}$; Ambion) using *HPRT*

577 (Forward 3'→5': CTTTCCTTGGTCAGGCAGTA, reverse 3'→5':

578 TGGCTTATATCCAACACTTCG) as an internal, endogenous control. Fold-change was

579 calculated using the $2^{-\Delta\Delta C_T}$ method and a One-Way ANOVA, Kruskal-Wallis test was performed

580 to determine statistical significance (GraphPad Prism v10).

581 **Ethics statement**

582 The human pancreas TMA and PDAC slides used in this study were approved by the

583 Georgetown University LCCC Biospecimen Use Committee.

584 **Supplementary Materials**

585 Supplementary Figure S1: Spatial proteomic analysis of the human PDAC TME resolves PDAC
586 cell populations.

587 Supplementary Figure S2: Subclustered cell populations of spatial proteomic resolved PDAC
588 cell populations.

589 Supplementary Figure S3: Proportions of PDAC subclustered cell populations per cellular
590 neighborhood.

591 Supplementary Figure S4: Pro-inflammatory NK cell and Macrophage Content is Inversely
592 Correlated with αSMA+ Fibroblasts.

593 Supplementary Figure S5: PDAC epithelial-ductal ROI cell type abundance.

594 Supplementary Figure S6: PDAC epithelial-ductal ROI cell subcluster abundance.

595 Supplementary Figure S7: NK cells retain expression of activator markers in fibroblast-rich
596 periductal regions.

597 Supplementary Figure S8: Subclustering of epithelial and fibroblast populations in human PDAC
598 scRNAseq samples.

599 Supplementary Figure S9: Fibroblast and epithelial cell populations exhibit differential
600 expression of CellChat-based collagen signaling genes.

601 Supplementary Figure S10: Human donor NK cells express CD44.

602 Supplementary Figure S11: CD44 neutralization increases human donor NK cell invasion into
603 PANC-1 PDAC spheroids.

604 Supplementary Figure S12: CD44 neutralization does not affect expression of MMP genes in
605 human donor NK cells.

606 Supplementary Table S1: IMC antibody panel and metal assignments.

607 Supplementary Table S2: PDAC patient information for IMC.

608 Supplementary Table S3: PDAC patient information for multiplex IF (Vectra®).

609 Supplementary Table S4: Antibodies and fluorescent dyes for multiplex IF (Vectra®).

610 Supplementary Table S5: MMP genes primer sequences.

611 **Acknowledgments**

612 We would like to thank the following from the Georgetown University Lombardi
613 Comprehensive Cancer Center's Shared Resources (SR) (partially supported by NIH/NCI
614 P30CA51008 grant): Dr. Karen Creswell, Dan Xu, and Zhinuo Jiang at the Flow Cytometry and
615 Cell Sorting SR (partially supported NIH S10OD016213 grant), Aaron Rozeboom, Bin Li, and
616 Dr. Susree Modepalli at the Histopathology and Tissue SR, Dr. Junfeng Ma at the Mass
617 Spectrometry and Analytical Pharmacology and the Biostatistics SR for support with performing
618 metal-conjugation, IMC, and multiplex immunohistochemistry, and with providing guidance on
619 spatial analyses. We would also like to thank the Tissue Culture and Biobanking and Microscopy
620 and Imaging Shared Resources for support on *in vitro* assays. We also thank Ahmed Elhossiny
621 and the Pasca Di Magliano lab at the University of Michigan for providing us with the
622 scRNAseq dataset for analyses described here. We also thank Drs. Andrew Quong and Eric
623 Swanson at Standard BioTools Inc. for assistance with the IMC antibody panel design and its
624 cell segmentation pipeline, and Dr. Ludmila Danilova at Johns Hopkins University for advice on
625 computational analyses. Schematics were created with BioRender.com.

626

627 **Author contributions**

628 Z.X.M., A.A.L., and L.M.W. conceived the idea, designed the study, obtained funding, and
629 wrote the manuscript. Z.X.M. and A.A.L. conducted experiments and analyzed the data. Z.X.M.,
630 A.A.L., R.K.S., A.D., S.A., and W.J.H. performed or assisted with computational analyses.
631 Z.X.M., R.K.S., and S.A. wrote R scripts and generated the computational figures. B.H. and
632 A.D. assisted with data collection and tissue pathology of human tissue samples. L.W. and M.C.
633 assisted in performing 2D *in vitro* invasion experiments. M.C. assisted with RT-qPCR, flow

634 cytometry assays, and 3D *in vitro* invasion experiments. I.P. and S.H. assisted in IMC data
635 collection. W.J.H., E.J.F., M.A., and S.A.J. assisted with experimental design. M.A., E.J.F, and
636 L.M.W. edited the manuscript. All authors critically reviewed and approved the manuscript.
637

638 **Competing interests**

639 Z.X.M. is currently employed by AstraZeneca. E.J.F. was on the scientific advisory board of
640 Resistance Bio and a consultant for Mestag Therapeutics. L.M.W. sits on the Scientific Advisory
641 Boards of Celldex Therapeutics, Bobcat Bio, Kuiper and Cytomx Therapeutics, is an advisor for
642 Fortress Biotech and is founder and Chair of the Board of PushCART Therapeutics.
643

644 **Code availability statement**

645 Code used to perform IMC and scRNAseq analyses and generate the figures is available at
646 https://github.com/Weiner-Lab/NaturalKillerCells_PDAC.
647

648 **Data transparency statement**

649 Code used to perform IMC and scRNAseq analyses and generate the figures is available at
650 https://github.com/Weiner-Lab/NaturalKillerCells_PDAC. Raw .mcd files for all cores of the
651 pancreas tissue microarray imaged by IMC and IMC-derived datasets, including histoCAT-
652 derived single cell files, and Seurat, SingleCellExperiment, Cytomapper and distance data matrix
653 R objects, to reproduce figures are deposited at doi: 10.5281/zenodo.10582038. Source Data are
654 provided with this paper. The scRNAseq data was provided to us by the Pasca Di Magliano lab
655 at the University of Michigan, which was previously published at doi: 10.1038/s43018-020-
656 00121-4. The authors declare that all other data supporting the findings of this study are available

657 within the paper or its supplementary information files. All other relevant data are available from
658 the corresponding author upon reasonable request.

659 **Funding**

660 This work is supported by grants from the National Institutes of Health, National Cancer Institute
661 T32CA009686 (Training Grant in Tumor Biology, Anna Tate Riegel), F31CA261125 (Z.X.M.),
662 F30CA294875 (A.A.L.), U24CA284156 (E.J.F.), and P30CA51008 (L.M.W), Achievement
663 Reward for College Scientists (ARCS) Foundation Scholar (Z.X.M.), and the Lustgarten
664 Foundation (E.J.F and W.J.H.).

References

(1) Siegel, R. L.; Giaquinto, A. N.; Jemal, A. Cancer statistics, 2024. *CA: a cancer journal for clinicians* **2024**, *74* (1), 12-49. DOI: 10.3322/caac.21820.

(2) Royal, R. E.; Levy, C.; Turner, K.; Mathur, A.; Hughes, M.; Kammula, U. S.; Sherry, R. M.; Topalian, S. L.; Yang, J. C.; Lowy, I. Phase 2 trial of single agent Ipilimumab (anti-CTLA-4) for locally advanced or metastatic pancreatic adenocarcinoma. *Journal of immunotherapy* **2010**, *33* (8), 828-833.

(3) Brahmer, J. R.; Tykodi, S. S.; Chow, L. Q.; Hwu, W.-J.; Topalian, S. L.; Hwu, P.; Drake, C. G.; Camacho, L. H.; Kauh, J.; Odunsi, K. Safety and activity of anti–PD-L1 antibody in patients with advanced cancer. *New England journal of medicine* **2012**, *366* (26), 2455-2465.

(4) O'Reilly, E. M.; Oh, D. Y.; Dhani, N.; Renouf, D. J.; Lee, M. A.; Sun, W.; Fisher, G.; Hezel, A.; Chang, S. C.; Vlahovic, G.; et al. Durvalumab With or Without Tremelimumab for Patients With Metastatic Pancreatic Ductal Adenocarcinoma: A Phase 2 Randomized Clinical Trial. *JAMA Oncol* **2019**, *5* (10), 1431-1438. DOI: 10.1001/jamaoncol.2019.1588 From NLM PubMed-not-MEDLINE.

(5) Karamitopoulou, E. Tumour microenvironment of pancreatic cancer: immune landscape is dictated by molecular and histopathological features. *British journal of cancer* **2019**, *121* (1), 5-14. DOI: 10.1038/s41416-019-0479-5.

(6) Muller, M.; Haghnejad, V.; Schaefer, M.; Gauchotte, G.; Caron, B.; Peyrin-Biroulet, L.; Bronowicki, J.-P.; Neuzillet, C.; Lopez, A. The immune landscape of human pancreatic ductal carcinoma: key players, clinical implications, and challenges. *Cancers* **2022**, *14* (4), 995. DOI: 10.3390/cancers14040995.

(7) Ferdek, P. E.; Jakubowska, M. A. Biology of pancreatic stellate cells—more than just pancreatic cancer. *Pflügers Archiv-European Journal of Physiology* **2017**, *469*, 1039-1050.

(8) Khaliq, A. M.; Rajamohan, M.; Saeed, O.; Mansouri, K.; Adil, A.; Zhang, C.; Turk, A.; Carstens, J. L.; House, M.; Hayat, S. Spatial transcriptomic analysis of primary and metastatic pancreatic cancers highlights tumor microenvironmental heterogeneity. *Nature genetics* **2024**, *56* (11), 2455-2465.

(9) Elyada, E.; Bolisetty, M.; Laise, P.; Flynn, W. F.; Courtois, E. T.; Burkhart, R. A.; Teinor, J. A.; Belleau, P.; Biffi, G.; Lucito, M. S. Cross-species single-cell analysis of pancreatic ductal adenocarcinoma reveals antigen-presenting cancer-associated fibroblasts. *Cancer discovery* **2019**, *9* (8), 1102-1123.

(10) Xu, Y.; Wang, X.; Li, Y.; Mao, Y.; Su, Y.; Mao, Y.; Yang, Y.; Gao, W.; Fu, C.; Chen, W. Multimodal single cell-resolved spatial proteomics reveal pancreatic tumor heterogeneity. *Nature Communications* **2024**, *15* (1), 10100.

(11) Sussman, J. H.; Kim, N.; Kemp, S. B.; Traum, D.; Katsuda, T.; Kahn, B. M.; Xu, J.; Kim, I.-K.; Eskandarian, C.; Delman, D. Multiplexed imaging mass cytometry analysis characterizes the vascular niche in pancreatic cancer. *Cancer research* **2024**, *84* (14), 2364-2376.

(12) Yousuf, S.; Qiu, M.; von Voithenberg, L. V.; Hulkkonen, J.; Macinkovic, I.; Schulz, A. R.; Hartmann, D.; Mueller, F.; Mijatovic, M.; Ibberson, D. Spatially resolved multi-omics single-cell analyses inform mechanisms of immune dysfunction in pancreatic cancer. *Gastroenterology* **2023**, *165* (4), 891-908. e814.

(13) Cui Zhou, D.; Jayasinghe, R. G.; Chen, S.; Herndon, J. M.; Iglesia, M. D.; Navale, P.; Wendl, M. C.; Caravan, W.; Sato, K.; Storrs, E. Spatially restricted drivers and transitional cell

populations cooperate with the microenvironment in untreated and chemo-resistant pancreatic cancer. *Nature genetics* **2022**, *54* (9), 1390-1405.
(14) Kim, S.; Leem, G.; Choi, J.; Koh, Y.; Lee, S.; Nam, S.-H.; Kim, J. S.; Park, C. H.; Hwang, H. K.; Min, K. I. Integrative analysis of spatial and single-cell transcriptome data from human pancreatic cancer reveals an intermediate cancer cell population associated with poor prognosis. *Genome medicine* **2024**, *16* (1), 20.
(15) Liudahl, S. M.; Betts, C. B.; Sivagnanam, S.; Morales-Oyarvide, V.; Da Silva, A.; Yuan, C.; Hwang, S.; Grossblatt-Wait, A.; Leis, K. R.; Larson, W. Leukocyte heterogeneity in pancreatic ductal adenocarcinoma: phenotypic and spatial features associated with clinical outcome. *Cancer discovery* **2021**, *11* (8), 2014-2031.
(16) Ene-Obong, A.; Clear, A. J.; Watt, J.; Wang, J.; Fatah, R.; Riches, J. C.; Marshall, J. F.; Chin-Aleong, J.; Chelala, C.; Gribben, J. G.; et al. Activated pancreatic stellate cells sequester CD8+ T cells to reduce their infiltration of the juxtatumoral compartment of pancreatic ductal adenocarcinoma. *Gastroenterology* **2013**, *145* (5), 1121-1132. DOI: 10.1053/j.gastro.2013.07.025 From NLM Medline.
(17) Bell, A. T.; Chianchiano, P.; Hirose, K.; Salas-Escabillas, D.; Zucha, D. M.; Mitchell, J. T.; Danilova, L.; Damanakis, A. I.; Tandurella, J. A.; Johnson, J. Spatial profiling of human pancreatic ductal adenocarcinoma reveals molecular alterations associated with venous invasion. *Science Translational Medicine* **2025**, *17* (817), eady7524.
(18) Bell, A. T.; Mitchell, J. T.; Kiemen, A. L.; Lyman, M.; Fujikura, K.; Lee, J. W.; Coyne, E.; Shin, S. M.; Nagaraj, S.; Deshpande, A. PanIN and CAF transitions in pancreatic carcinogenesis revealed with spatial data integration. *Cell Systems* **2024**, *15* (8), 753-769. e755.
(19) Biffi, G.; Oni, T. E.; Spielman, B.; Hao, Y.; Elyada, E.; Park, Y.; Preall, J.; Tuveson, D. A. IL1-induced JAK/STAT signaling is antagonized by TGFβ to shape CAF heterogeneity in pancreatic ductal adenocarcinoma. *Cancer discovery* **2019**, *9* (2), 282-301.
(20) Oh, K.; Yoo, Y. J.; Torre-Healy, L. A.; Rao, M.; Fassler, D.; Wang, P.; Caponegro, M.; Gao, M.; Kim, J.; Sasson, A. Coordinated single-cell tumor microenvironment dynamics reinforce pancreatic cancer subtype. *Nature communications* **2023**, *14* (1), 5226.
(21) Niu, N.; Shen, X.; Wang, Z.; Chen, Y.; Weng, Y.; Yu, F.; Tang, Y.; Lu, P.; Liu, M.; Wang, L. Tumor cell-intrinsic epigenetic dysregulation shapes cancer-associated fibroblasts heterogeneity to metabolically support pancreatic cancer. *Cancer Cell* **2024**, *42* (5), 869-884. e869.
(22) Ligorio, M.; Sil, S.; Malagon-Lopez, J.; Nieman, L. T.; Misale, S.; Di Pilato, M.; Ebright, R. Y.; Karabacak, M. N.; Kulkarni, A. S.; Liu, A. Stromal microenvironment shapes the intratumoral architecture of pancreatic cancer. *Cell* **2019**, *178* (1), 160-175. e127.
(23) Steele, N. G.; Carpenter, E. S.; Kemp, S. B.; Sirihorachai, V. R.; The, S.; Delrosario, L.; Lazarus, J.; Amir, E.-a. D.; Gunchick, V.; Espinoza, C. Multimodal mapping of the tumor and peripheral blood immune landscape in human pancreatic cancer. *Nature cancer* **2020**, *1* (11), 1097-1112. DOI: 10.1038/s43018-020-00121-4.
(24) Chang, Q.; Ornatsky, O. I.; Siddiqui, I.; Loboda, A.; Baranov, V. I.; Hedley, D. W. Imaging mass cytometry. *Cytometry part A* **2017**, *91* (2), 160-169. DOI: 10.1002/cyto.a.23053.
(25) Butler, A.; Hoffman, P.; Smibert, P.; Papalexi, E.; Satija, R. Integrating single-cell transcriptomic data across different conditions, technologies, and species. *Nature biotechnology* **2018**, *36* (5), 411-420.

(26) Stuart, T.; Butler, A.; Hoffman, P.; Hafemeister, C.; Papalexi, E.; Mauck, W. M.; Hao, Y.; Stoeckius, M.; Smibert, P.; Satija, R. Comprehensive integration of single-cell data. *cell* **2019**, *177* (7), 1888-1902. e1821.
(27) Hao, Y.; Hao, S.; Andersen-Nissen, E.; Mauck, W. M.; Zheng, S.; Butler, A.; Lee, M. J.; Wilk, A. J.; Darby, C.; Zager, M. Integrated analysis of multimodal single-cell data. *Cell* **2021**, *184* (13), 3573-3587. e3529. DOI: 10.1016/j.cell.2021.04.048.
(28) Schapiro, D.; Jackson, H. W.; Raghuraman, S.; Fischer, J. R.; Zanotelli, V. R.; Schulz, D.; Giesen, C.; Catena, R.; Varga, Z.; Bodenmiller, B. histoCAT: analysis of cell phenotypes and interactions in multiplex image cytometry data. *Nature methods* **2017**, *14* (9), 873-876. DOI: 10.1038/nmeth.4391.
(29) Satija, R.; Farrell, J. A.; Gennert, D.; Schier, A. F.; Regev, A. Spatial reconstruction of single-cell gene expression data. *Nature biotechnology* **2015**, *33* (5), 495-502.
(30) Hafemeister, C.; Satija, R. Normalization and variance stabilization of single-cell RNA-seq data using regularized negative binomial regression. *Genome biology* **2019**, *20* (1), 296. DOI: 10.1186/s13059-019-1874-1.
(31) Schürch, C. M.; Bhate, S. S.; Barlow, G. L.; Phillips, D. J.; Noti, L.; Zlobec, I.; Chu, P.; Black, S.; Demeter, J.; McIlwain, D. R. Coordinated cellular neighborhoods orchestrate antitumoral immunity at the colorectal cancer invasive front. *Cell* **2020**, *182* (5), 1341-1359. e1319. DOI: 10.1016/j.cell.2020.07.005.
(32) Gocher, A. M.; Workman, C. J.; Vignali, D. A. Interferon-γ: teammate or opponent in the tumour microenvironment? *Nature Reviews Immunology* **2022**, *22* (3), 158-172.
(33) Ho, W. J.; Zhu, Q.; Durham, J.; Popovic, A.; Xavier, S.; Leatherman, J.; Mohan, A.; Mo, G.; Zhang, S.; Gross, N. Neoadjuvant cabozantinib and nivolumab convert locally advanced hepatocellular carcinoma into resectable disease with enhanced antitumor immunity. *Nature Cancer* **2021**, *2* (9), 891-903. DOI: 10.1038/s43018-021-00234-4.
(34) Lee, H.; Ferguson, A. L.; Quek, C.; Vergara, I. A.; Pires daSilva, I.; Allen, R.; Gide, T. N.; Conway, J. W.; Koufariotis, L. T.; Hayward, N. K. Intratumoral CD16+ macrophages are associated with clinical outcomes of patients with metastatic melanoma treated with combination anti-PD-1 and anti-CTLA-4 therapy. *Clinical Cancer Research* **2023**, *29* (13), 2513-2524.
(35) Fauriat, C.; Long, E. O.; Ljunggren, H.-G.; Bryceson, Y. T. Regulation of human NK-cell cytokine and chemokine production by target cell recognition. *Blood, The Journal of the American Society of Hematology* **2010**, *115* (11), 2167-2176.
(36) Öhlund, D.; Handly-Santana, A.; Biffi, G.; Elyada, E.; Almeida, A. S.; Ponz-Sarvise, M.; Corbo, V.; Oni, T. E.; Hearn, S. A.; Lee, E. J. Distinct populations of inflammatory fibroblasts and myofibroblasts in pancreatic cancer. *Journal of Experimental Medicine* **2017**, *214* (3), 579-596.
(37) Chen, Y.; Kim, J.; Yang, S.; Wang, H.; Wu, C.-J.; Sugimoto, H.; LeBleu, V. S.; Kalluri, R. Type I collagen deletion in αSMA+ myofibroblasts augments immune suppression and accelerates progression of pancreatic cancer. *Cancer cell* **2021**, *39* (4), 548-565. e546. DOI: 10.1016/j.ccell.2021.02.007.
(38) Lanier, L. L. NKG2D receptor and its ligands in host defense. *Cancer immunology research* **2015**, *3* (6), 575-582.
(39) Carstens, J. L.; Correa de Sampaio, P.; Yang, D.; Barua, S.; Wang, H.; Rao, A.; Allison, J. P.; LeBleu, V. S.; Kalluri, R. Spatial computation of intratumoral T cells correlates with

survival of patients with pancreatic cancer. *Nat Commun* **2017**, *8*, 15095. DOI: 10.1038/ncomms15095 From NLM Medline.
(40) Jin, S.; Guerrero-Juarez, C. F.; Zhang, L.; Chang, I.; Ramos, R.; Kuan, C.-H.; Myung, P.; Plikus, M. V.; Nie, Q. Inference and analysis of cell-cell communication using CellChat. *Nature communications* **2021**, *12* (1), 1088. DOI: 10.1038/s41467-021-21246-9.
(41) Gulati, G. S.; Sikandar, S. S.; Wesche, D. J.; Manjunath, A.; Bharadwaj, A.; Berger, M. J.; Ilagan, F.; Kuo, A. H.; Hsieh, R. W.; Cai, S. Single-cell transcriptional diversity is a hallmark of developmental potential. *Science* **2020**, *367* (6476), 405-411. DOI: 10.1126/science.aax0249.
(42) Enane, F. O.; Saunthararajah, Y.; Korc, M. Differentiation therapy and the mechanisms that terminate cancer cell proliferation without harming normal cells. *Cell death & disease* **2018**, *9* (9), 912. DOI: 10.1038/s41419-018-0919-9.
(43) Zhang, T.; Ren, Y.; Yang, P.; Wang, J.; Zhou, H. Cancer-associated fibroblasts in pancreatic ductal adenocarcinoma. *Cell Death Dis* **2022**, *13* (10), 897. DOI: 10.1038/s41419-022-05351-1 From NLM Medline.
(44) Wang, Y.; Liang, Y.; Xu, H.; Zhang, X.; Mao, T.; Cui, J.; Yao, J.; Wang, Y.; Jiao, F.; Xiao, X. Single-cell analysis of pancreatic ductal adenocarcinoma identifies a novel fibroblast subtype associated with poor prognosis but better immunotherapy response. *Cell discovery* **2021**, *7* (1), 36.
(45) Clark, R. A.; Alon, R.; Springer, T. A. CD44 and hyaluronan-dependent rolling interactions of lymphocytes on tonsillar stroma. *The Journal of cell biology* **1996**, *134* (4), 1075-1087.
(46) Hughes, C. S.; Postovit, L. M.; Lajoie, G. A. Matrigel: a complex protein mixture required for optimal growth of cell culture. *Proteomics* **2010**, *10* (9), 1886-1890.
(47) Chen, C.; Zhao, S.; Karnad, A.; Freeman, J. W. The biology and role of CD44 in cancer progression: therapeutic implications. *Journal of hematology & oncology* **2018**, *11*, 1-23. DOI: 10.1186/s13045-018-0605-5.
(48) McMahon, M.; Ye, S.; Pedrina, J.; Dlugolenski, D.; Stambas, J. Extracellular matrix enzymes and immune cell biology. *Frontiers in Molecular Biosciences* **2021**, *8*, 703868. DOI: 10.3389/fmolb.2021.703868.
(49) Feig, C.; Jones, J. O.; Kraman, M.; Wells, R. J.; Deonarine, A.; Chan, D. S.; Connell, C. M.; Roberts, E. W.; Zhao, Q.; Caballero, O. L. Targeting CXCL12 from FAP-expressing carcinoma-associated fibroblasts synergizes with anti–PD-L1 immunotherapy in pancreatic cancer. *Proceedings of the National Academy of Sciences* **2013**, *110* (50), 20212-20217.
(50) Paavola, K. J.; Roda, J. M.; Lin, V. Y.; Chen, P.; O'Hollaren, K. P.; Ventura, R.; Crawley, S. C.; Li, B.; Chen, H.-I. H.; Malmersjö, S. The fibronectin–ILT3 interaction functions as a stromal checkpoint that suppresses myeloid cells. *Cancer immunology research* **2021**, *9* (11), 1283-1297.
(51) Özdemir, B. C.; Pentcheva-Hoang, T.; Carstens, J. L.; Zheng, X.; Wu, C.-C.; Simpson, T. R.; Laklai, H.; Sugimoto, H.; Kahlert, C.; Novitskiy, S. V. Depletion of carcinoma-associated fibroblasts and fibrosis induces immunosuppression and accelerates pancreas cancer with reduced survival. *Cancer cell* **2014**, *25* (6), 719-734.
(52) Van Cutsem, E.; Tempero, M. A.; Sigal, D.; Oh, D.-Y.; Fazio, N.; Macarulla, T.; Hitre, E.; Hammel, P.; Hendifar, A. E.; Bates, S. E. Randomized phase III trial of pegvorhyaluronidase alfa with nab-paclitaxel plus gemcitabine for patients with hyaluronan-

high metastatic pancreatic adenocarcinoma. *Journal of Clinical Oncology* **2020**, *38* (27), 3185-3194.

(53) Delgado-Gonzalez, A.; Sanchez-Martin, R. M. Mass cytometry tags: where chemistry meets single-cell analysis. *Analytical Chemistry* **2020**, *93* (2), 657-664. DOI: 10.1021/acs.analchem.0c03560.

(54) Windhager, J.; Zanotelli, V. R. T.; Schulz, D.; Meyer, L.; Daniel, M.; Bodenmiller, B.; Eling, N. An end-to-end workflow for multiplexed image processing and analysis. *Nature Protocols* **2023**, 1-49. DOI: 10.1038/s41596-023-00881-0.

(55) Lee, C.-W.; Ren, Y. J.; Marella, M.; Wang, M.; Hartke, J.; Couto, S. S. Multiplex immunofluorescence staining and image analysis assay for diffuse large B cell lymphoma. *Journal of immunological methods* **2020**, *478*, 112714. DOI: 10.1016/j.jim.2019.112714.

(56) Bankhead, P.; Loughrey, M. B.; Fernández, J. A.; Dombrowski, Y.; McArt, D. G.; Dunne, P. D.; McQuaid, S.; Gray, R. T.; Murray, L. J.; Coleman, H. G. QuPath: Open source software for digital pathology image analysis. *Scientific reports* **2017**, *7* (1), 1-7.

(57) Schmidt, U.; Weigert, M.; Broaddus, C.; Myers, G. Cell detection with star-convex polygons. In *International conference on medical image computing and computer-assisted intervention*, 2018; Springer: pp 265-273.

(58) Scrucca, L.; Fop, M.; Murphy, T. B.; Raftery, A. E. mclust 5: clustering, classification and density estimation using Gaussian finite mixture models. *The R journal* **2016**, *8* (1), 289. DOI: 10.32614/RJ-2016-021.

(59) Zahavi, D. J.; Erbe, R.; Zhang, Y.-W.; Guo, T.; Malchiodi, Z. X.; Maynard, R.; Lekan, A.; Gallagher, R.; Wulfkuhle, J.; Petricoin, E. Antibody dependent cell-mediated cytotoxicity selection pressure induces diverse mechanisms of resistance. *Cancer Biology & Therapy* **2023**, *24* (1), 2269637. DOI: 10.1080/15384047.2023.2269637.

(60) Ajina, R.; Malchiodi, Z. X.; Fitzgerald, A. A.; Zuo, A.; Wang, S.; Moussa, M.; Cooper, C. J.; Shen, Y.; Johnson, Q. R.; Parks, J. M. Antitumor T-cell immunity contributes to pancreatic cancer immune resistance. *Cancer immunology research* **2021**, *9* (4), 386-400.

(61) Carr, W. H.; Zinsou, C.; Rowe, T.; Lange, C.; Lawal, O. O. Human natural killer cell expansion in vitro using mitomycin-C treatment as an alternative to irradiation of modified K562 feeder cells. *The Journal of Immunology* **2017**, *198* (1_Supplement), 82.16-82.16. DOI: 10.4049/jimmunol.198.Supp.82.16.

(62) Schindelin, J.; Arganda-Carreras, I.; Frise, E.; Kaynig, V.; Longair, M.; Pietzsch, T.; Preibisch, S.; Rueden, C.; Saalfeld, S.; Schmid, B. Fiji: an open-source platform for biological-image analysis. *Nature methods* **2012**, *9* (7), 676-682. DOI: 10.1038/nmeth.2019.

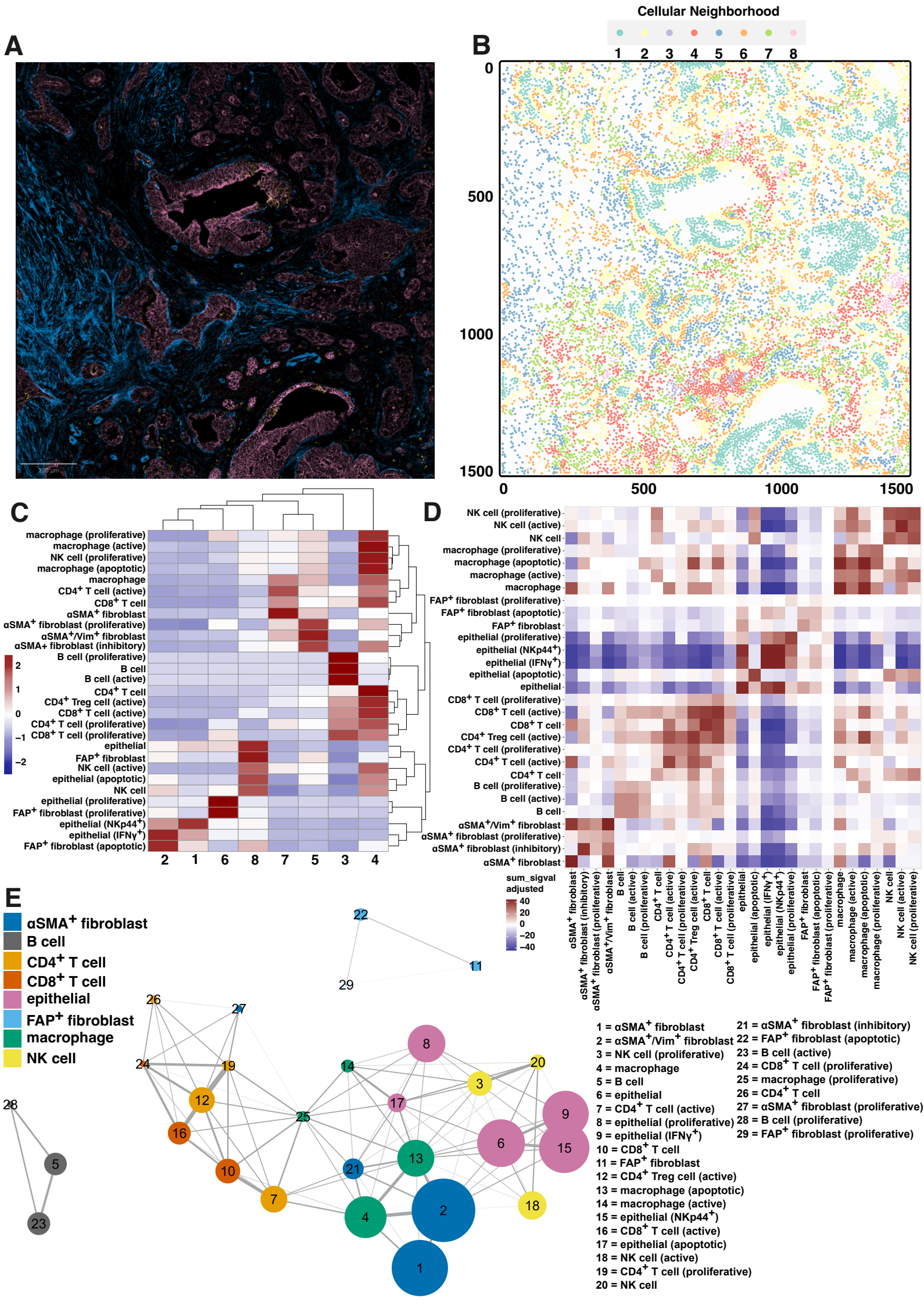
A
B
Cellular Neighborhood
1 2 3 4 5 6 7 8
0
500
1000
1500
C
macrophage (proliferative)
macrophage (active)
NK cell (proliferative)
macrophage (apoptotic)
macrophage
CD4+ T cell (active)
CD8+ T cell
αSMA+ fibroblast
αSMA+ fibroblast (proliferative)
αSMA+/Vim+ fibroblast
αSMA+ fibroblast (inhibitory)
B cell (proliferative)
B cell
B cell (active)
CD4+ T cell
CD4+ Treg cell (active)
CD8+ T cell (active)
CD4+ T cell (proliferative)
CD8+ T cell (proliferative)
epithelial
FAP+ fibroblast
NK cell (active)
epithelial (apoptotic)
NK cell
epithelial (proliferative)
FAP+ fibroblast (proliferative)
epithelial (NKp44+)
epithelial (IFNγ+)
FAP+ fibroblast (apoptotic)
2 1 6 8 7 5 3 4
2
1
0
−1
−2
D
sum_sigval adjusted
40
20
0
−20
−40
E
αSMA+ fibroblast
B cell
CD4+ T cell
CD8+ T cell
epithelial
FAP+ fibroblast
macrophage
NK cell
1 = αSMA+ fibroblast
2 = αSMA+/Vim+ fibroblast
3 = NK cell (proliferative)
4 = macrophage
5 = B cell
6 = epithelial
7 = CD4+ T cell (active)
8 = epithelial (proliferative)
9 = epithelial (IFNγ+)
10 = CD8+ T cell
11 = FAP+ fibroblast
12 = CD4+ Treg cell (active)
13 = macrophage (apoptotic)
14 = macrophage (active)
15 = epithelial (NKp44+)
16 = CD8+ T cell (active)
17 = epithelial (apoptotic)
18 = NK cell (active)
19 = CD4+ T cell (proliferative)
20 = NK cell
21 = αSMA+ fibroblast (inhibitory)
22 = FAP+ fibroblast (apoptotic)
23 = B cell (active)
24 = CD8+ T cell (proliferative)
25 = macrophage (proliferative)
26 = CD4+ T cell
27 = αSMA+ fibroblast (proliferative)
28 = B cell (proliferative)
29 = FAP+ fibroblast (proliferative)

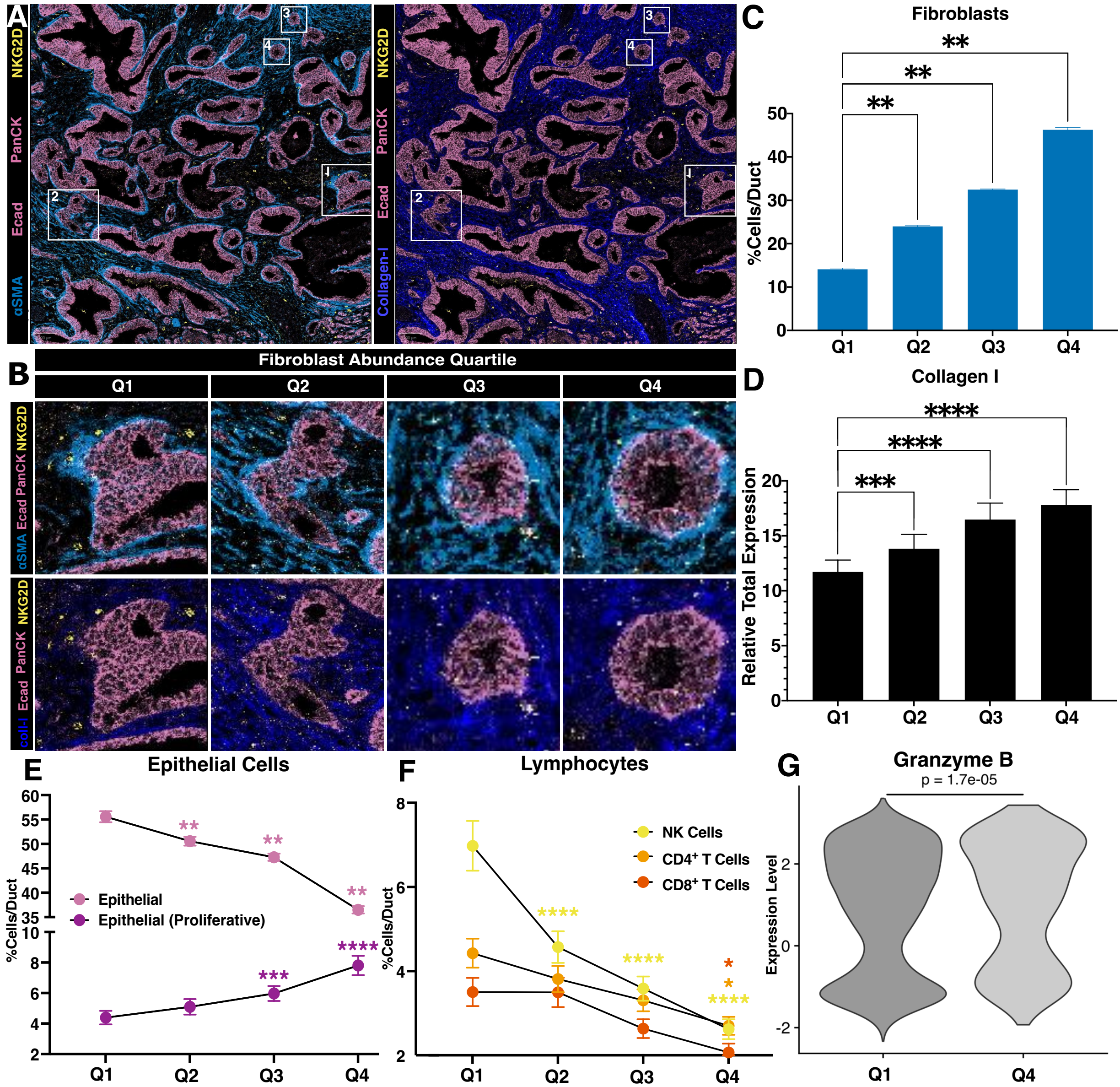
A
NKG2D
PanCK
Ecad
αSMA
Collagen-I
B
Fibroblast Abundance Quartile
Q1
Q2
Q3
Q4
αSMA Ecad PanCK NKG2D
coll-I Ecad PanCK NKG2D
C
Fibroblasts
%Cells/Duct
D
Collagen I
Relative Total Expression
E
Epithelial Cells
%Cells/Duct
Epithelial
Epithelial (Proliferative)
F
Lymphocytes
%Cells/Duct
NK Cells
CD4+ T Cells
CD8+ T Cells
G
Granzyme B
p = 1.7e-05
Expression Level

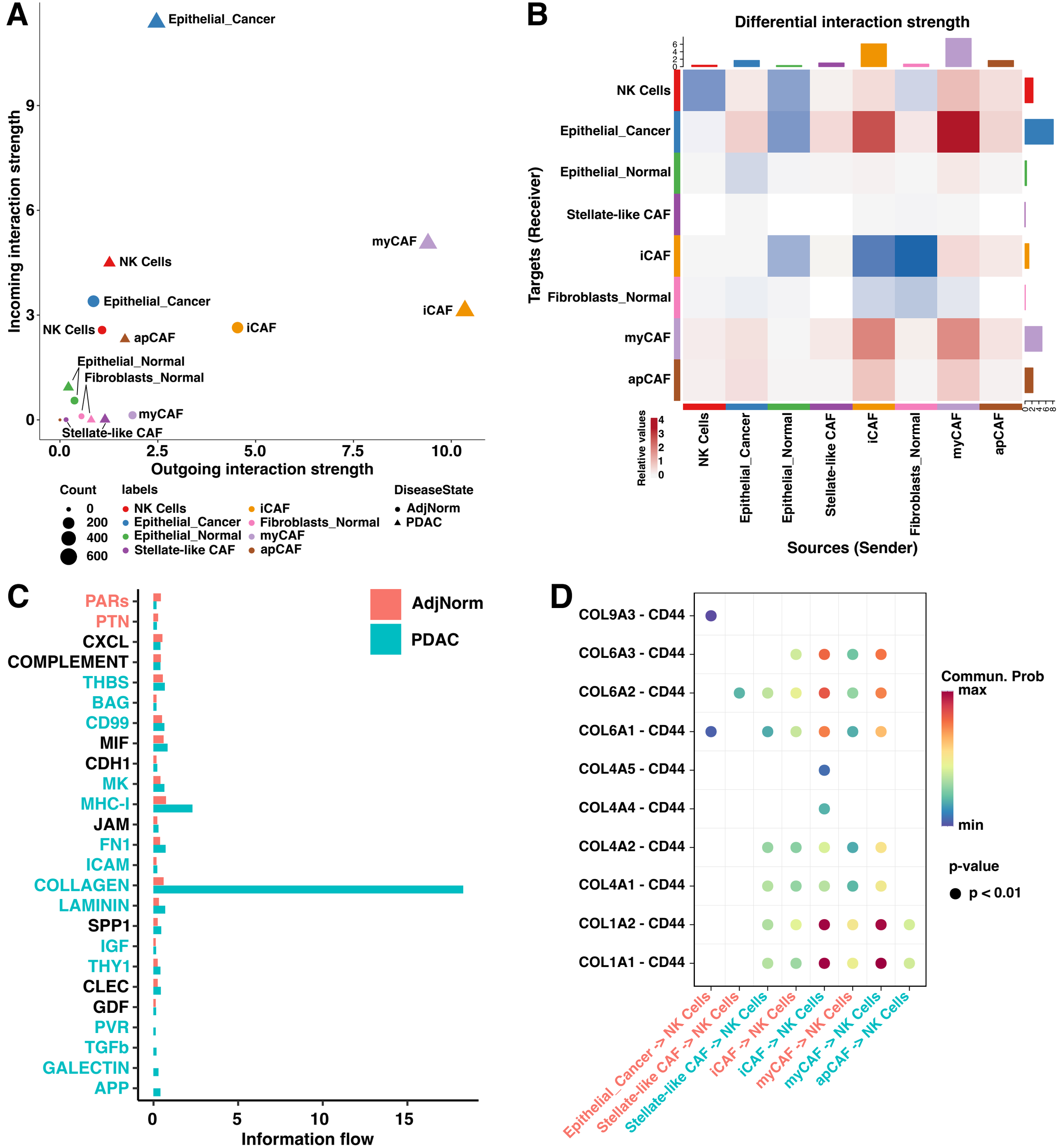
A
Incoming interaction strength
Outgoing interaction strength
Epithelial_Cancer
NK Cells
Epithelial_Cancer
NK Cells
apCAF
iCAF
myCAF
iCAF
Epithelial_Normal
Fibroblasts_Normal
myCAF
Stellate-like CAF
Count
0
200
400
600
labels
NK Cells
Epithelial_Cancer
Epithelial_Normal
Stellate-like CAF
iCAF
Fibroblasts_Normal
myCAF
apCAF
DiseaseState
AdjNorm
PDAC
B
Differential interaction strength
Targets (Receiver)
NK Cells
Epithelial_Cancer
Epithelial_Normal
Stellate-like CAF
iCAF
Fibroblasts_Normal
myCAF
apCAF
Relative values
Sources (Sender)
C
PARs
PTN
CXCL
COMPLEMENT
THBS
BAG
CD99
MIF
CDH1
MK
MHC-I
JAM
FN1
ICAM
COLLAGEN
LAMININ
SPP1
IGF
THY1
CLEC
GDF
PVR
TGFb
GALECTIN
APP
AdjNorm
PDAC
Information flow
D
COL9A3 - CD44
COL6A3 - CD44
COL6A2 - CD44
COL6A1 - CD44
COL4A5 - CD44
COL4A4 - CD44
COL4A2 - CD44
COL4A1 - CD44
COL1A2 - CD44
COL1A1 - CD44
Epithelial_Cancer -> NK Cells
Stellate-like CAF -> NK Cells
Stellate-like CAF -> NK Cells
iCAF -> NK Cells
iCAF -> NK Cells
myCAF -> NK Cells
myCAF -> NK Cells
apCAF -> NK Cells
Commun. Prob
max
min
p-value
p < 0.01

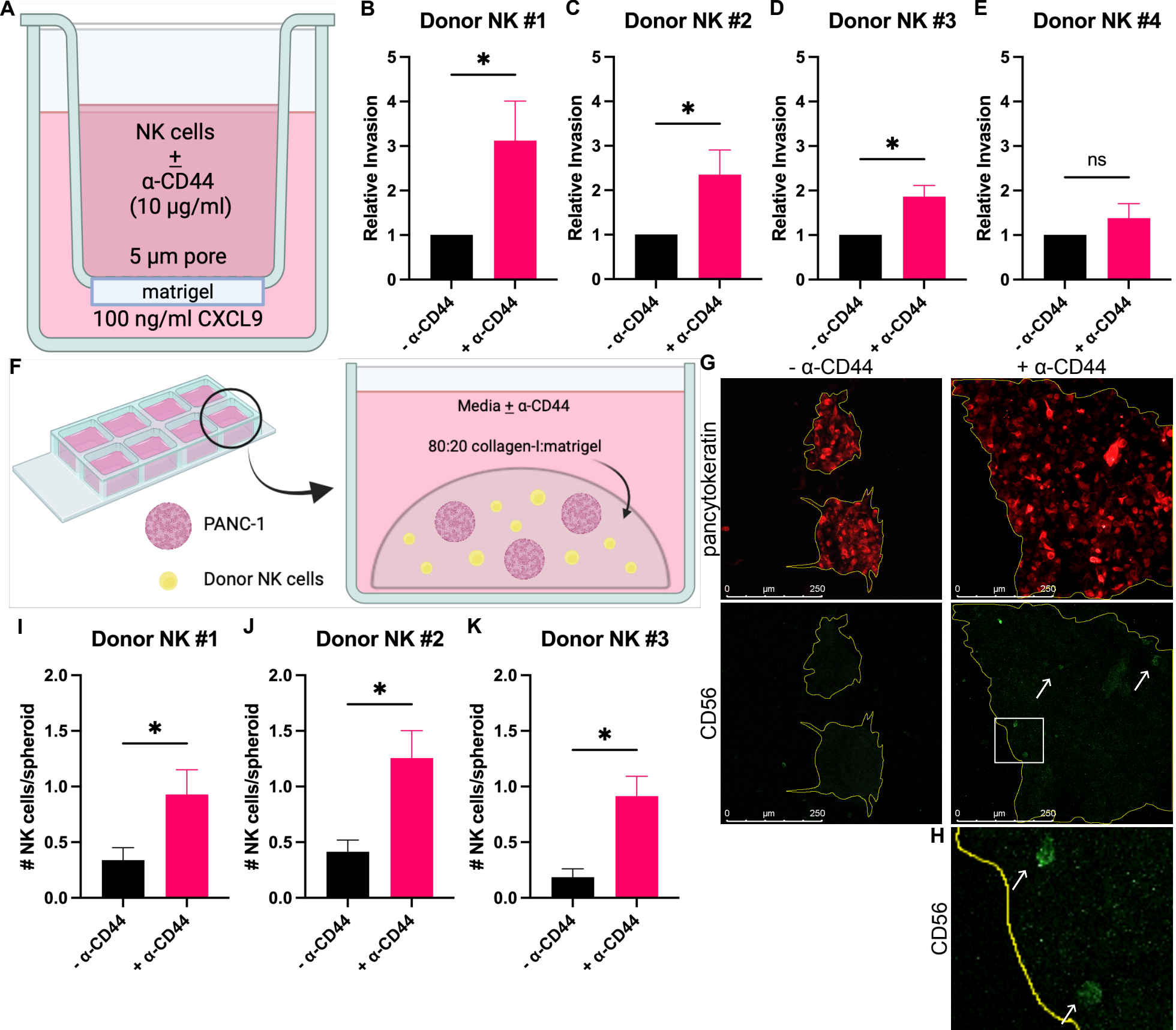
A
NK cells
±
α-CD44
(10 µg/ml)
5 µm pore
matrigel
100 ng/ml CXCL9
B
Donor NK #1
C
Donor NK #2
D
Donor NK #3
E
Donor NK #4
Relative Invasion
*
ns
- α-CD44
+ α-CD44
F
Media ± α-CD44
80:20 collagen-I:matrigel
PANC-1
Donor NK cells
G
- α-CD44
+ α-CD44
pancytokeratin
CD56
0 µm 250
H
CD56
I
Donor NK #1
J
Donor NK #2
K
Donor NK #3
NK cells/spheroid